

REVIEW ARTICLE

Open Access

Surface atomic-layer superconductors with Rashba/Zeeman-type spin-orbit coupling



Takashi Uchihashi

Abstract

In this article, we review the recent progress in surface atomic-layer superconductors on semiconductor substrates with Rashba/Zeeman-type spin-orbit coupling (SOC). After introduction of some of the basics of Rashba/Zeeman-type SOC and its effects on superconductivity, representative surface structures with relevant features are described in terms of their crystalline and electronic properties. This is followed by recent experimental studies that have revealed anomalous superconducting phenomena, which can be attributed to the effects of Rashba/Zeeman-type SOC. Future prospects, likely to be driven by instrumental developments, are given as a concluding remark.

Keywords: Surface, Atomic layer, Superconductor, Rashba/Zeeman-type Spin-orbit coupling, Inversion-symmetry breaking

1 Introduction

Since the discovery of two-dimensional (2D) superconductors with atomic-scale thickness and well-defined crystallinity, the research has seen a tremendous growth in number and in diversity, involving many kinds of superconducting materials and state-of-the-art technologies [1, 2]. For example, various kinds of atomically thin layered materials such as transition-metal dichalcogenides and high transition-temperature (T_c) cuprates have been fabricated by molecular beam epitaxy, liquid-ion gating, mechanical exfoliation, and van der Waals heterostructure assembling [3–8]. These studies have demonstrated that superconductivity can indeed exist in the atomic-scale 2D limit against a naive expectation. Surprisingly, superconductivity is sometimes induced or strongly enhanced in this regime as revealed in FeSe monolayers on SrTiO₃ and twisted bilayer graphene with moiré patterns [4, 7].

Among all, surface atomic-layer superconductors on semiconductor substrates [9–15], one of the earliest discoveries in this family, are considered prototypical 2D superconductors due to their simple chemical and

crystal structures. They typically consist of one or two layers of metal atoms chemically adsorbed on a clean semiconductor surface, featuring crystal symmetries, and electronic structures distinct from those of the bulk counterparts. Due to the ultrahigh vacuum environment usually required, their fundamental microscopic properties can be readily accessed through surface-sensitive techniques such as scanning tunneling microscopy (STM) [14, 16–19]. This makes a sharp contrast to other kinds of 2D superconductors, which are mostly confined to a buried interface and thus cannot be probed with such techniques. One of the important aspects of surface atomic layers is the fact that they are coupled to the substrate with chemical bonds. This inevitably breaks the inversion symmetry of the crystal and induces asymmetric charge distribution in the out-of-plane direction, which leads to Rashba-type spin-orbit coupling (SOC) [20–27]. Important consequences of Rashba-type SOC are the lifting of the spin degeneracy of electronic bands and resulting spin polarizations in the momentum space, which is referred to as the Rashba effects. For surface atomic layers on semiconductors, the Rashba effects have directly been observed through angle-resolved photoemission spectroscopy (ARPES) and spin-resolved ARPES (SARPES) [28–32].

Correspondence: UCHIHASHI.Takashi@nims.go.jp

International Center for Materials Nanoarchitectonics (WPI-MANA), National Institute for Materials Science (NIMS), 1-1, Namiki, Tsukuba, Ibaraki 305-0044, Japan



© The Author(s). 2021 **Open Access** This article is licensed under a Creative Commons Attribution 4.0 International License, which permits use, sharing, adaptation, distribution and reproduction in any medium or format, as long as you give appropriate credit to the original author(s) and the source, provide a link to the Creative Commons licence, and indicate if changes were made. The images or other third party material in this article are included in the article's Creative Commons licence, unless indicated otherwise in a credit line to the material. If material is not included in the article's Creative Commons licence and your intended use is not permitted by statutory regulation or exceeds the permitted use, you will need to obtain permission directly from the copyright holder. To view a copy of this licence, visit <http://creativecommons.org/licenses/by/4.0/>.

Notably, superconductivity can strongly be influenced by the presence of Rashba-type SOC, because Cooper pair formation is sensitive to the spin splitting of the Fermi surface. Very exotic phenomena caused by Rashba-type SOC have already been predicted, e.g., singlet-triplet mixing in Cooper pairs [33, 34], supercurrent-induced spin polarization and its inverse effect [35–38], enhanced critical magnetic field due to the suppression of the Pauli paramagnetism [34, 36, 38, 39], and superconducting states with a spatially modulated order parameter [40–44]. Experimental investigations on these novel phenomena have already started with non-centrosymmetric heavy-fermion superconductors in bulk forms [45–49], but evidence for them has often been elusive. This is partly due to the complexity of the electronic/magnetic states of the target materials and difficulties in preparing high-quality single crystals or films. By contrast, surface atomic layers are simple in terms of their crystalline structures and chemical compositions, and their electronic states are understandable without considering complex correlation effects. Their ideal 2D character originating from the ultimate atomic-scale thickness is also advantageous because one can safely neglect the electron orbital effects in the out-of-plane direction. Therefore, the surface atomic layers are potentially regarded as model superconductors with Rashba-type SOC.

In this review article, we introduce the recent progress in surface atomic-layer superconductors with Rashba-type SOC. The topics also include closely related Zeeman-type SOC, which is often found for surface atomic layers. Although the development of the field treated here is still in the nascent stage, our trial should stimulate researchers in both surface science and superconductivity communities and will hopefully bridge the gap between them. The present paper is organized as follows. In Section 2, we explain some of the very basics of Rashba/Zeman-type SOC and its effects on superconductivity. Section 3 introduces representative surface atomic-layers superconductors with Rashba/Zeman-type SOC. In Section 4, we elaborate recent experimental studies related to the present topics. Finally, the future prospect is described in Section 5.

2 Rashba/Zeman-type SOC and its effects on superconductivity

2.1 Basics of Rashba/Zeman-type SOC

The quantum states of electrons in a crystal are governed by the symmetries of the system. Let us consider a one-electron state with crystal momentum \mathbf{k} (referred to as momentum for simplicity) and spin α ($\alpha = \uparrow, \downarrow$), the eigenenergy of which is $E(\mathbf{k}, \alpha)$. If the crystal has the inversion symmetry, a relation $E(-\mathbf{k}, \alpha) = E(\mathbf{k}, \alpha)$ holds because the parity operation applies only to the orbital

degree of freedom. By contrast, if the system has the time reversal symmetry (i.e., no magnetic field or exchange interaction), a relation $E(-\mathbf{k}, -\alpha) = E(\mathbf{k}, \alpha)$ holds since the time-reversal operation applies to both the orbital and spin degrees of freedom. These two equations lead to a relation $E(\mathbf{k}, -\alpha) = E(\mathbf{k}, \alpha)$, requiring that the electronic states in a system with both inversion and time-reversal symmetries are always spin-degenerate [50].

If the inversion symmetry of the crystal is absent, the above relation does not hold anymore, i.e. $E(\mathbf{k}, -\alpha) \neq E(\mathbf{k}, \alpha)$, due to the presence of spin-orbit coupling (SOC) in general. Nevertheless, for the states with $\mathbf{k} = 0$, $E(0, -\alpha) = E(0, \alpha)$ is guaranteed from the time-reversal relation and thus these states are spin degenerate. This special relation is not only applied to the states with $\mathbf{k} = 0$ but also to those with a time reversal invariant momentum (TRIM), which is defined as a momentum \mathbf{q} that satisfies a relation $-\mathbf{q} + \mathbf{G} = \mathbf{q}$ (\mathbf{G} is a reciprocal lattice vector). Because of this relation, $E(\mathbf{q}, -\alpha) = E(-\mathbf{q}, \alpha) = E(-\mathbf{q} + \mathbf{G}, \alpha) = E(\mathbf{q}, \alpha)$ holds. As \mathbf{k} is moved away from a TRIM point, the degeneracy of the two states with the same \mathbf{k} but the opposite spins is lifted and the energy separation increases.

Let us consider a 2D surface system with a square or triangular lattice, whose 2D Brillouin zone is depicted in Fig. 1a. Since the inversion symmetry is broken on the surface in the normal direction, the band degeneracy should be generally lifted around the TRIM points. For a small electron momentum \mathbf{k} near the $\bar{\Gamma}$ point, the band splitting is described by the following Hamiltonian [51]

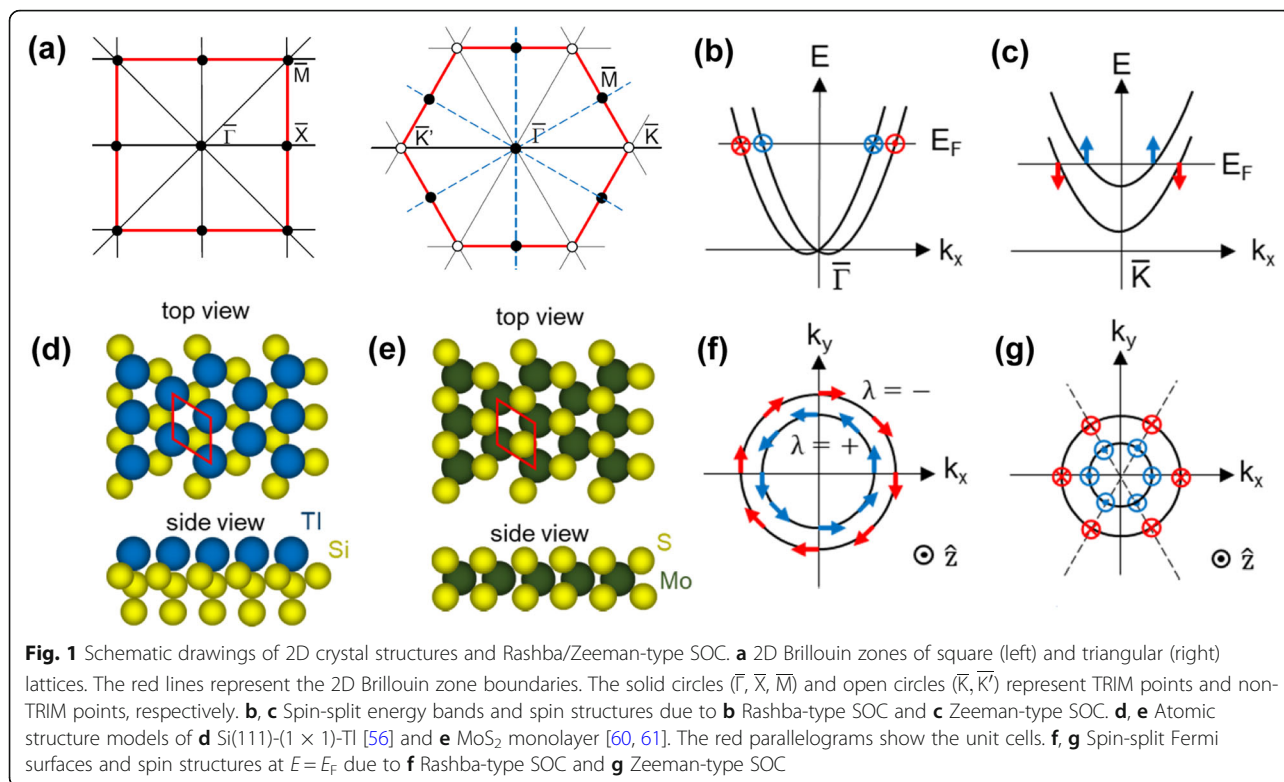
$$H = \frac{\hbar^2 k^2}{2m^*} + H_R \quad (1)$$

$$H_R \equiv \alpha_R (\hat{\mathbf{z}} \times \mathbf{k}) \cdot \boldsymbol{\sigma} \quad (2)$$

where $k = |\mathbf{k}|$, m^* is electron effective mass, α_R is the Rashba parameter, $\hat{\mathbf{z}}$ is the unit vector in the normal direction, and $\boldsymbol{\sigma}$ is the Pauli matrix for spin. The interaction described by Eq. (2) is called the Rashba-type SOC, which was first applied to Wurtzite crystals and the 2D electron gas formed at AlGaAs/GaAs heterostructures by Rashba and coworkers [20, 21]. The eigenenergy of this Hamiltonian can be obtained as

$$E^\pm(k) = \frac{\hbar^2 k^2}{2m^*} \pm \alpha_R k \quad (3)$$

(Fig. 1b). The energy splitting on the Fermi surface (FS) ΔE_F is equal to $2\alpha_R k_F$, where k_F is the Fermi wave-number. The corresponding eigenstates are spin-polarized states with the spin quantization axes fixed perpendicular to both \mathbf{k} and $\hat{\mathbf{z}}$ within the 2D plane. The



sign \pm in Eq. (3), denoted as band helicity λ , corresponds to the spin direction. Accordingly, the FS splits into two concentric circles with chiral spin polarization structures (Fig. 1f). This type of band degeneracy lifting is called the Rashba-type spin-splitting. Depending on the symmetry of the system, it can be found not only around $\bar{\Gamma}$ point but also around other TRIM¹. The size and sign of α_R are dependent on actual material parameters of the relevant system, and ΔE_F can be as large as 100 meV–1 eV when the surface consists of heavy elements [23, 25]. This huge value cannot be explained by a simple 2D free-electron model, and is attributed to a large SOC at the composing atoms and to the asymmetry of charge distribution around the nuclei of the topmost layer [24, 26]. Furthermore, orbital angular momentum localized on atomic sites plays a crucial role in real materials [27, 52].

For large k values, the spin-split FSs are not circular anymore because of higher-order k terms added in the energy dispersion in Eq. (3) [53]. Furthermore, for many kinds of surface 2D crystals, the inversion symmetry is broken not only in the out-of-plane direction but also in the in-plane directions. This allows the presence of the out-of-plane component in spin polarization vectors in

general, in contrast to the ideal Rashba-type spin splitting. The details of band splitting and spin structure are dependent on crystal symmetry, relevant electronic band, TRIM point, etc. [29, 49, 51, 53, 54], but the spin splitting is often called “Rashba-type” if its structure is analogous to the one described above.

The atomic layers on Si(111) or Ge(111) surfaces with (1 × 1) periodicity, for which the in-plane inversion center is lacking, have interesting properties arising from the symmetry of plane group p3m1 (e.g., see Fig. 1d) for the atomic structure of Si(111)-(1 × 1)-TI [51, 55, 56]. Among the high-symmetry points in its Brillouin zone (Fig. 1a), the \bar{K} and \bar{K}' points are not TRIM points since the relation $-\mathbf{q} + \mathbf{G} = \mathbf{q}$ does not hold, and a Rashba-type splitting is absent there. Instead, a new “Zeeman-type” spin splitting (and SOC) exists due to the C_3 symmetry of these points². Namely, the electronic band is split in energy without crossing at the \bar{K}/\bar{K}' point, and spin polarizations at the split bands are opposite and align precisely in the out-of-plane direction (Fig. 1,c g). The Zeeman-type SOC can be described by a Hamiltonian of the form

$$H_z(\mathbf{k} + \mathbf{cK}) \equiv \epsilon\beta\hat{z} \cdot \boldsymbol{\sigma} \quad (4)$$

¹The Rashba-type spin splitting exists around the \bar{K} point for a triangular lattice with the symmetry of plane group p31m, although the \bar{K} point is not a TRIM point [29, 51].

²Zeeman-type SOC is also called Ising(-type) SOC in the field of superconductivity.

where $\epsilon = \pm 1$ is the valley index corresponding to the \bar{K} and \bar{K}' points, \mathbf{K} is the momentum of the \bar{K} point, and β is the strength of Zeeman-type SOC [57–59]. Notably, Zeeman-type spin splittings also exist for MoS₂ and NbSe₂ monolayers fabricated by liquid-ion gating or mechanical exfoliation [6, 59–61]. In contrast to their bulk counterparts, monolayers with the half-unit cell thickness lack the inversion symmetry in the in-plane direction and belongs to plane group p3m1 (e.g., see Fig. 1e) for the atomic structure of MoS₂ monolayer). At the \bar{K}/\bar{K}' point of the Brillouin zone, only a Zeeman-type spin splitting is allowed due to its symmetry.

The effect that the spin polarization direction is fixed by the momentum of the electron is called spin-momentum locking³. The difference in spin polarization directions for Rashba- and Zeeman-type SOC plays an important role when considering the response of a 2D superconductor to strong magnetic fields, as will be discussed in Section 2.2.2 and Section 4.2.

2.2 The effects of Rashba/Zeeman-type SOC on superconductivity

The studies on the influences of Rashba-type SOC on superconductivity can be traced back to the work by Edelstein. For a superconductor with a Rashba-type spin splitting, Edelstein predicted spin-singlet/triplet mixing in Cooper pairs [33] and current-induced magnetization (spin polarization) [35] exactly like in a normal metal [62]. Since then, a variety of phenomena caused by Rashba/Zeeman-type SOC have been investigated theoretically. In the following, some of the main results are presented while focusing on their basic concepts. For more comprehensive reviews, the readers are referred to Ref. [38, 48, 49, 63].

2.2.1 Singlet-triplet mixing in Cooper pairs

For a superconductor with the inversion symmetry, it is well known that Cooper pairs can be classified into two kinds: a spin-singlet state with an even-parity orbital wavefunction and a spin-triplet state with an odd-parity orbital wavefunction. Namely, if the orbital part is even (odd) in terms of exchange of two particles, it requires the spin part to be odd (even) due to the fermionic nature of electrons. This means that the Cooper pair is a spin-singlet (spin-triplet) state. The conventional Bardeen-Cooper-Schrieffer (BCS)-type superconductors have spin-singlet Cooper pairs with an s-wave orbital. However, if the inversion symmetry of the system is

broken, the spin singlet and triplet states can be mixed because of SOC [33, 34, 39–41]. We show below how such a pairing can be allowed by following the treatment of Ref. [63].

Let us consider the free-electron-like FS with a Rashba-type spin splitting, for which the inner and outer bands are denoted by helicities $\lambda = \pm$ (Fig. 2a). Since the spin is locked perpendicular to the momentum, the states with momentum \mathbf{k} for the $\lambda = \pm$ bands are expressed as

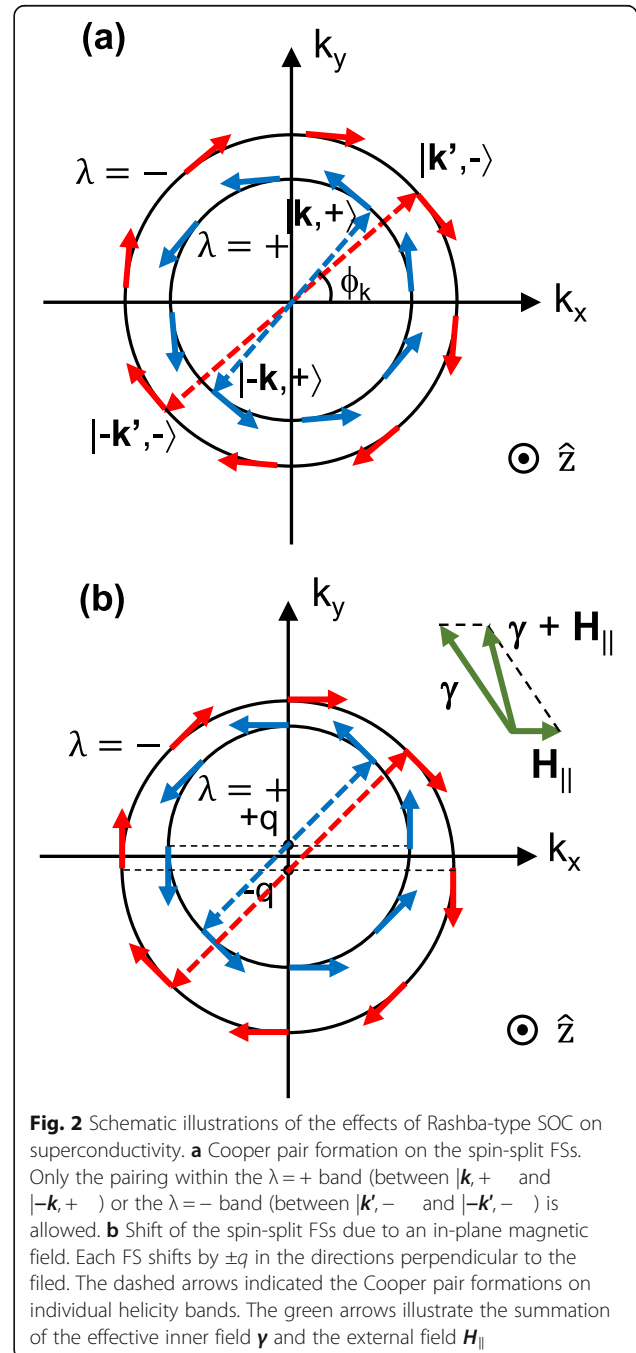


Fig. 2 Schematic illustrations of the effects of Rashba-type SOC on superconductivity. **a** Cooper pair formation on the spin-split FS. Only the pairing within the $\lambda = +$ band (between $|\mathbf{k}, +\rangle$ and $|\mathbf{-k}, +\rangle$) or the $\lambda = -$ band (between $|\mathbf{k}', -\rangle$ and $|\mathbf{-k}', -\rangle$) is allowed. **b** Shift of the spin-split FSs due to an in-plane magnetic field. Each FS shifts by $\pm q$ in the directions perpendicular to the field. The dashed arrows indicated the Cooper pair formations on individual helicity bands. The green arrows illustrate the summation of the effective inner field $\boldsymbol{\gamma}$ and the external field \mathbf{H}_{\parallel}

³For the system with Zeeman-type SOC, it is also called spin-valley locking because the spin direction is determined by the valley index of the \bar{K}/\bar{K}' point. In the present paper, for simplicity, we refer to all the spin locking mechanism due to the Rashba/Zeeman-type SOC as spin-momentum locking.

$$|\mathbf{k}, +\rangle = (|\mathbf{k}, \uparrow\rangle + ie^{i\phi_{\mathbf{k}}}|\mathbf{k}, \downarrow\rangle)/\sqrt{2} \quad (5)$$

$$|\mathbf{k}, -\rangle = (ie^{-i\phi_{\mathbf{k}}}|\mathbf{k}, \uparrow\rangle + |\mathbf{k}, \downarrow\rangle)/\sqrt{2} \quad (6)$$

where $\uparrow\downarrow$ indicates up and down spins along the z axis and $\phi_{\mathbf{k}}$ is the azimuthal angle of \mathbf{k} . Eqs. (5) and (6) are also expressed as

$$a_{\mathbf{k}+}^{\dagger} = (a_{\mathbf{k}\uparrow}^{\dagger} + ie^{i\phi_{\mathbf{k}}}a_{\mathbf{k}\downarrow}^{\dagger})/\sqrt{2} \quad (7)$$

$$a_{\mathbf{k}-}^{\dagger} = (ie^{-i\phi_{\mathbf{k}}}a_{\mathbf{k}\uparrow}^{\dagger} + a_{\mathbf{k}\downarrow}^{\dagger})/\sqrt{2} \quad (8)$$

where $a_{\mathbf{k}\pm}^{\dagger}$, $a_{\mathbf{k}\uparrow}^{\dagger}$, $a_{\mathbf{k}\downarrow}^{\dagger}$ are the creation operators for the states $|\mathbf{k}, \pm\rangle$, $|\mathbf{k}, \uparrow\rangle$, $|\mathbf{k}, \downarrow\rangle$, respectively. While Cooper pairs are formed by pairing $|\mathbf{k}, \uparrow\rangle$ and $|\mathbf{k}, \downarrow\rangle$ (also $|\mathbf{k}, \downarrow\rangle$ and $|\mathbf{k}, \uparrow\rangle$) in the conventional superconductor, they involve pairings between the states on the same helicity band for a Rashba-split system: $|\mathbf{k}, +\rangle$ and $|\mathbf{k}, -\rangle$ for the $\lambda = +$ band, and $|\mathbf{k}', -\rangle$ and $|\mathbf{k}', +\rangle$ for the $\lambda = -$ band (see the dashed arrows in Fig. 2(a)). This leads to an effective pairing Hamiltonian of the form

$$H_{\text{pair}} = \sum_{\mathbf{k}} \{ \Delta_{+}(\mathbf{k}) ie^{-i\phi_{\mathbf{k}}} a_{\mathbf{k}+}^{\dagger} a_{-\mathbf{k}-}^{\dagger} + \Delta_{-}(\mathbf{k}) \times (-ie^{-i\phi_{\mathbf{k}}}) a_{\mathbf{k}-}^{\dagger} a_{-\mathbf{k}+}^{\dagger} \} + \text{h.c.} \quad (9)$$

where $\Delta_{\pm}(\mathbf{k})$ denote the pair potentials for $\lambda = \pm$ pairings and h.c. stands for Hermitian conjugate. Here, the phase factors $\pm ie^{\mp i\phi_{\mathbf{k}}}$ are inserted for convenience. By substituting Eqs. (7) and (8), we arrive at a Hamiltonian of the form

$$\begin{aligned} H_{\text{pair}} &= \sum_{\mathbf{k}} (a_{\mathbf{k}\uparrow}^{\dagger}, a_{\mathbf{k}\downarrow}^{\dagger}) \begin{pmatrix} \frac{\Delta_{+}(\mathbf{k}) - \Delta_{-}(\mathbf{k})}{2} e^{-i\phi_{\mathbf{k}}} & \frac{\Delta_{+}(\mathbf{k}) + \Delta_{-}(\mathbf{k})}{2} \\ -\frac{\Delta_{+}(\mathbf{k}) + \Delta_{-}(\mathbf{k})}{2} & \frac{\Delta_{+}(\mathbf{k}) - \Delta_{-}(\mathbf{k})}{2} e^{i\phi_{\mathbf{k}}} \end{pmatrix} \begin{pmatrix} a_{-\mathbf{k}\uparrow}^{\dagger} \\ a_{-\mathbf{k}\downarrow}^{\dagger} \end{pmatrix} + \text{h.c.} \\ &= \sum_{\mathbf{k}} (a_{\mathbf{k}\uparrow}^{\dagger}, a_{\mathbf{k}\downarrow}^{\dagger}) \{ \phi(i\sigma_y) + \mathbf{d} \cdot (i\sigma_y) \} \begin{pmatrix} a_{-\mathbf{k}\uparrow}^{\dagger} \\ a_{-\mathbf{k}\downarrow}^{\dagger} \end{pmatrix} + \text{h.c.} \\ &\quad \text{where} \\ &\quad \phi \equiv \frac{\Delta_{+}(\mathbf{k}) + \Delta_{-}(\mathbf{k})}{2} \\ &\quad \mathbf{d} \equiv \frac{\Delta_{+}(\mathbf{k}) - \Delta_{-}(\mathbf{k})}{2} (-\sin\phi_{\mathbf{k}}, \cos\phi_{\mathbf{k}}, 0) \end{aligned} \quad (10)$$

are the pair potentials for the spin singlet and triplet components, respectively. If $\Delta_{+}(\mathbf{k}) = \Delta_{-}(\mathbf{k})$, the Cooper pair is a pure singlet state, but singlet and triplet states can be mixed in general. Note that \mathbf{d} is parallel to the spin quantization direction $(-\sin\phi_{\mathbf{k}}, \cos\phi_{\mathbf{k}}, 0)$. The result fulfills the condition required for the triplet component to persist in a superconductor without inversion symmetry [39].

2.2.2 Suppression of the Pauli paramagnetism and enhancement of critical magnetic field

When a strong magnetic field is applied to a conventional type II superconductor, vortex supercurrents are generated. The increase in kinetic energy due to the currents suppresses superconductivity and completely destroys it at the upper critical field H_{c2} . This mechanism is called the orbital pair-breaking effect. However, when an in-plane field is applied to an atomically thin 2D superconductor, this orbital effect is nearly absent because supercurrents cannot run in the out-of-plane direction. In this case, spin-singlet Cooper pairs are destroyed by so-called paramagnetic pair breaking effect, i.e., by field-induced parallel alignment of electron spins. At $T = 0$, this occurs when the paramagnetic energy gain acquired by a transition to the normal state becomes equal to the superconducting condensation energy [64, 65]. Denoting the critical field as H_p for this mechanism, the condition is expressed as

$$\frac{1}{2}\chi_{0n}H_p^2 - \frac{1}{2}\chi_{0s}H_p^2 = \frac{1}{2}N(0)\Delta(0)^2 \quad (11)$$

Here, χ_{0n} and χ_{0s} are the paramagnetic susceptibility in the normal and superconducting states, respectively, $N(0)$ is the density of states per spin at the Fermi level, and $\Delta(0)$ is the superconducting energy gap at $T = 0$. For a metal, χ_{0n} is given by Pauli paramagnetic susceptibility $\chi_P = 2\mu_B^2N(0)$, and $\chi_{0s} = 0$ at $T = 0$ for spin-singlet states. From these relations, one obtains the critical field H_p as

$$\mu_B H_p = \frac{1}{\sqrt{2}} \Delta(0) \quad (12)$$

The H_p determined from Eq. (12) is called the Pauli (or Clogston-Chandrasekhar) limit. For a BCS superconductor, H_p amounts to 1.86 T for $T_c = 1$ K ($\Delta(0) = 1.76 k_B T_c$). This result can be strongly modified by the presence of the Rashba/Zeeman-type SOC and the spin-momentum locking (see Section 2.1) as shown below.

In the case of the Zeeman-type SOC, which locks spin polarization in the out-of-plane direction (Fig. 1c, g), the in-plane critical field $H_{c2\parallel}$ can be drastically enhanced beyond the Pauli limit H_p [34, 36, 39]. This is because the Zeeman energy $\mu_B \boldsymbol{\sigma} \cdot \mathbf{H}$ is zero when the spin magnetic moment $-\mu_B \boldsymbol{\sigma}$ is locked perpendicular to the applied field \mathbf{H} . Namely, the Pauli paramagnetism is absent even in the normal state. Nevertheless, the spin can be slightly tilted toward the field direction by the second-order Perturbation due to the $\mu_B \boldsymbol{\sigma} \cdot \mathbf{H}$ term. When integrated over the whole occupied \mathbf{k} states, the shift in spin direction leads to a susceptibility equal to χ_P . This mechanism is referred to as Van Vleck paramagnetism⁴. The susceptibility χ_V in this case is essentially constant for both normal and superconducting states, i.e., $\chi_{0n} = \chi_{0s} =$

χ_P , if the splitting energy is much larger than the superconducting energy gap. Therefore, $H_{c2\parallel} \rightarrow \infty$ at $T = 0$ is deduced from the Eq. (11).

In the case of Rashba-type SOC, the above mechanism is applicable to an out-of-plane magnetic field because the spin polarizations are confined in the in-plane directions in this case (Fig. 1b, f). If the orbital pair-breaking is absent by some reason (e.g., by extremely large effective electron mass [38]), one obtains the critical magnetic field $H_{c2\perp} \rightarrow \infty$ at $T = 0$. However, for an in-plane magnetic field, the $H_{c2\parallel}$ enhancement effect is much weaker. Since the spin rotates as a function of the azimuthal angle ϕ_k of the momentum \mathbf{k} , Van Vleck paramagnetism dominates over the Pauli counterpart only in the region where \mathbf{k} is nearly perpendicular to \mathbf{H} . In this region, $\chi_{0n} \approx \chi_{0s} \approx \chi_P$. By contrast, for the region where \mathbf{k} is nearly parallel to \mathbf{H} , Pauli paramagnetism dominates over the Van Vleck counterpart, i.e. $\chi_{0n} \approx \chi_P$ and $\chi_{0s} \approx 0$. The integration over the \mathbf{k} states results in an equal contribution from the Pauli and Van Vleck paramagnetisms, i.e., $\chi_{0n} = \chi_P$ and $\chi_{0s} = \chi_P/2$. Therefore, one obtains $H_{c2\parallel} = \sqrt{2} H_P$ at $T = 0$ from the Eq. (11) [34, 36].

2.2.3 Spatially modulated superconducting states

When an in-plane magnetic field \mathbf{H}_{\parallel} is applied to a system with Rashba-type spin-splitting, it couples with the electron spins through the Zeeman energy. Since the spin direction is locked perpendicular to the momentum \mathbf{k} in a Rashba system, it leads to a shift of the spin-split Fermi surface (FS) in the momentum space in two opposite directions (Fig. 2b) [43, 66]. In the superconducting state, this coupling induces unique spatial modulations of the order parameter as shown below.

Let us consider Rashba-type spin-split FSs of a 2D free-electron system described by the Hamiltonians of Eqs. (1) and (2). The Rashba Hamiltonian can be expressed as $H_R = \mu_B \boldsymbol{\sigma} \cdot \boldsymbol{\gamma}$ if one defines an effective internal field by $\boldsymbol{\gamma} \equiv \alpha_R (\hat{\mathbf{z}} \times \mathbf{k}) / \mu_B$. With the addition of the external field \mathbf{H}_{\parallel} , the total effective field becomes $\boldsymbol{\gamma} + \mathbf{H}_{\parallel}$. If the Rashba splitting energy $\mu_B |\boldsymbol{\gamma}|$ is much larger than the Zeeman energy $\mu_B |\mathbf{H}_{\parallel}|$, the energy dispersion for band helicity \pm is given by [40, 48]

$$\begin{aligned} \epsilon_{\pm}(\mathbf{k}, \mathbf{H}_{\parallel}) &\approx \frac{\hbar^2 k^2}{2m^*} \pm \mu_B |\boldsymbol{\gamma}| \pm \mu_B \hat{\boldsymbol{\gamma}} \cdot \mathbf{H}_{\parallel} \\ &= \frac{\hbar^2 k^2}{2m^*} \pm \mu_B |\boldsymbol{\gamma}| \mp \mu_B (\hat{\mathbf{z}} \times \mathbf{H}_{\parallel}) \cdot \hat{\mathbf{k}} \end{aligned} \quad (13)$$

where $\hat{\boldsymbol{\gamma}}$ and $\hat{\mathbf{k}}$ are the unit vectors along $\boldsymbol{\gamma}$ and \mathbf{k} , respectively. By requiring the condition $\epsilon_{\pm}(\mathbf{k} + \mathbf{q}, \mathbf{H}_{\parallel}) = \epsilon_{\pm}(\mathbf{k}, \mathbf{H}_{\parallel} = 0)$, the shift of the FS \mathbf{q} is determined to be

$$\mathbf{q} \approx \pm \frac{\mu_B}{\hbar v_F} \hat{\mathbf{z}} \times \mathbf{H}_{\parallel}, \quad |\mathbf{q}| \approx \frac{\mu_B H_{\parallel}}{\hbar v_F}. \quad (14)$$

where $v_F \equiv \hbar k_F / m^*$ is the Fermi velocity. The FSs with the helicities \pm shift in opposite directions perpendicular to \mathbf{H}_{\parallel} . Since $\epsilon_{\pm}(\mathbf{k} + \mathbf{q}, \mathbf{H}_{\parallel}) = \epsilon_{\pm}(\mathbf{k}, \mathbf{H}_{\parallel} = 0) = \epsilon_{\pm}(-\mathbf{k}, \mathbf{H}_{\parallel} = 0) = \epsilon_{\pm}(-\mathbf{k} + \mathbf{q}, \mathbf{H}_{\parallel})$, Cooper pairs may be formed within each FS between the states $\mathbf{k} + \mathbf{q}$ and $-\mathbf{k} + \mathbf{q}$ at strong fields above $\sim H_P$ (see the dashed arrows in Fig. 2(b)). This leads to the formation of Cooper pairs with finite momentum $\pm 2\mathbf{q}$, with a spatial modulation of the order parameter in the form of $\Psi(\mathbf{r}) \propto \{\exp(i2\mathbf{q} \cdot \mathbf{r}) + \exp(-i2\mathbf{q} \cdot \mathbf{r})\}/2 = \cos(2\mathbf{q} \cdot \mathbf{r})$ [40, 43, 66]. This state is analogous to the Fulde-Ferrell-Larkin-Ovchinnikov (FFLO) state realized without Rashba-type SOC [67, 68], and is often called by the same name.

When the FFLO state is absent at low magnetic fields or destroyed by impurity scatterings, the competition between the two spin-split FSs becomes important. The relative difference in the density of states on the FSs in the order of $\alpha_R / \hbar v_F$ leads to a spatial modulation of the order parameter in the form of $\Psi(\mathbf{r}) \propto \exp(i2\mathbf{q}' \cdot \mathbf{r})$ [41–44, 66]. The wavevector \mathbf{q}' is given by

$$|\mathbf{q}'| = |\mathbf{q}| \frac{\alpha_R}{\hbar v_F} \approx \frac{\mu_B H_{\parallel} \alpha_R}{\hbar^2 v_F^2}, \quad \mathbf{q}' \parallel \hat{\mathbf{z}} \times \mathbf{H}_{\parallel} \quad (15)$$

This spatially modulated superconducting state is called the helical state. The helical state is closely related to the supercurrent induced by magnetoelectric effect of Rashba-type SOC, which is also proportional to $\alpha_R / \hbar v_F$ [36]. This supercurrent is driven by the in-plane magnetic field \mathbf{H}_{\parallel} in the direction of $\hat{\mathbf{z}} \times \mathbf{H}_{\parallel}$, but there also exists a counter supercurrent running in the opposite direction due to the phase gradient of the helical phase. These two currents cancel with each other in an isolated system [43].

3 Surface atomic-layer superconductors with Rashba/Zeeman-type SOC

In this section, representative surface atomic layers with Rashba/Zeeman-type SOC are described in terms of their basic crystalline and electronic structures. The emergence of superconductivity at low temperatures, through either an intrinsic phase transition or the proximity effect, has been confirmed for these materials. Here, 1 ML of an adsorbed layer is defined as a nominal coverage corresponding to one atom per (1×1) unit cell of the underlying substrate. Periodicity is also taken against the (1×1) unit cell of the substrate.

3.1 Ge(111)- $\beta(\sqrt{3} \times \sqrt{3})$ -Pb

This surface structure consists of a single atomic layer of Pb grown on the Ge(111) surface, with the resulting periodicity of $(\sqrt{3} \times \sqrt{3})$ (nominal coverage of Pb = 4/

⁴Conventionally, Van Vleck paramagnetism refers to the magnetism of atoms, ions, etc. without magnetic moments, which is derived by the second order perturbation due to the Zeeman interaction.

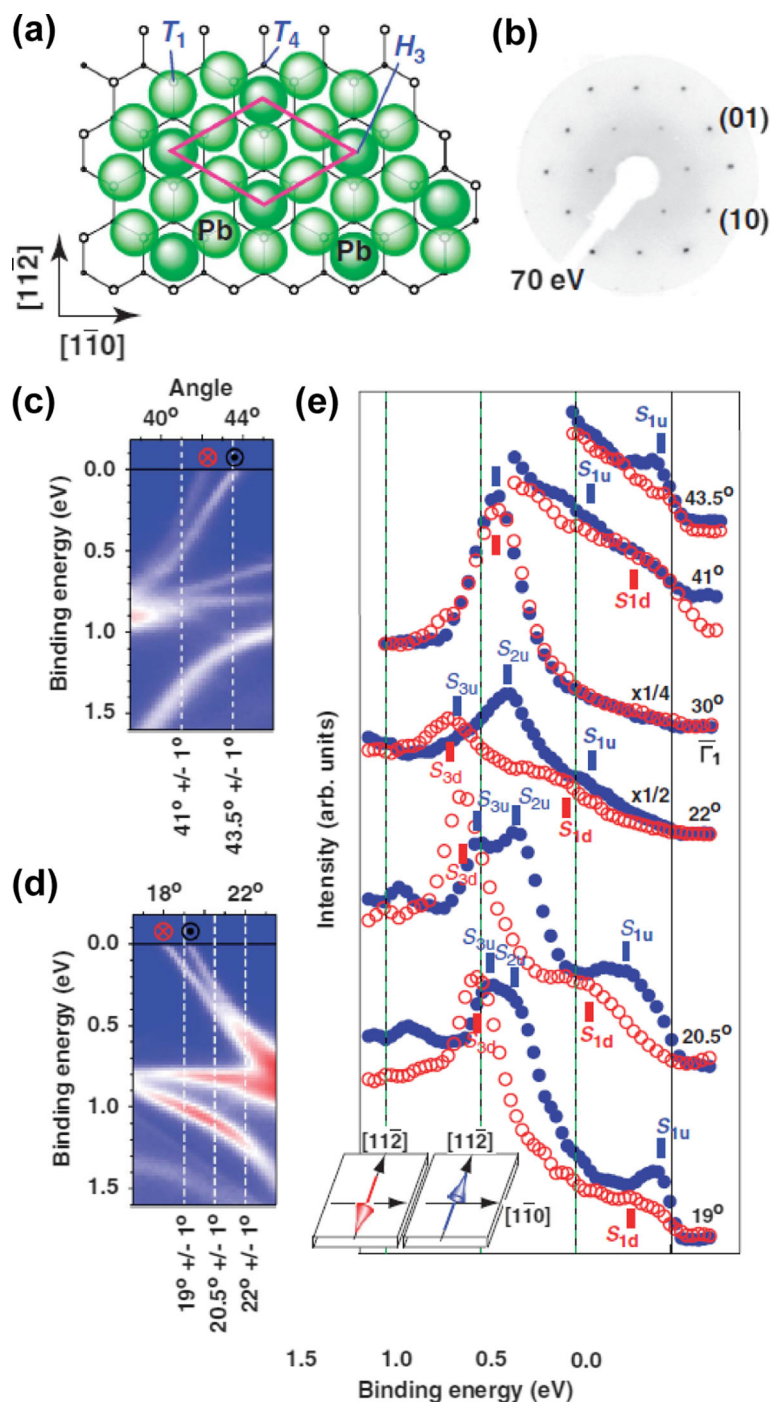


Fig. 3 Crystalline and electronic structures of Ge(111)- $\beta(\sqrt{3} \times \sqrt{3})$ -Pb. **a** Atomic structure model. **b** Low energy electron diffraction (LEED) pattern. **c, d** Spin-unpolarized ARPES spectra. **e** Spin-resolved ARPES spectra measured at several selected angles. Reprinted by permission from Macmillan Publishers Ltd.: K. Yaji, et al. Nat. Commun. 1, 17 (2010) [28], copyright 2010. <http://dx.doi.org/10.1038/ncomms1016>

3 ML) (Fig. 3a, b) [28, 69, 70]. The Pb layer resembles a close-packed triangular lattice but deviates from it due to the influence of the substrate. One of the four Pb atoms per unit cell is located at the hollow site (H_3 site) of the Ge(111) surface, forming a tetramer together with

the other three Pb atoms. The total crystal structure belongs to plane group $p31m$ (point group C_{3v}). The presence of heavy element of Pb on the top surface indicates a large Rashba-type spin splitting for this surface, which was experimentally demonstrated through ARPES and

SARPES measurements [28]. Large hexagonally-shaped FSs around the $\bar{\Gamma}$ point have clearly been observed with an energy splitting of ~ 200 meV, and the detected chiral spin structure is typical of a Rashba system (Fig. 3c–e). Nevertheless, large out-of-plane spin components was also predicted based on ab initio calculations [71], reflecting the absence of a mirror plane along the $\bar{\Gamma}$ – \bar{M} direction [26].

Ge(111)- $\beta(\sqrt{3} \times \sqrt{3})$ -Pb is the first example of metal atomic layers on a semiconductor surface with Rashba-type spin-split FS. The combination of the metallic surface and the semiconducting (i.e., insulating at low temperatures) substrate allows one to search for superconductivity in this system. It retains a metallic behavior at very low temperatures, but does not exhibit a superconducting transition down to 0.5 K [72, 73]. Nevertheless, it is possible to induce superconductivity in Ge(111)- $\beta(\sqrt{3} \times \sqrt{3})$ -Pb through the proximity effect when isolated Pb islands are grown on top of it, as revealed by electron transport and STS measurements [73, 74]. (Note that Ge(111)-SIC-Pb observed in Ref. [74] consists of spatially modulated Ge(111)- $\beta(\sqrt{3} \times \sqrt{3})$ -Pb domains.) Considering the well-characterized FS with a huge Rashba-type spin splitting, the present system can be an excellent candidate for studying a 2D superconductor with a strong Rashba effect.

3.2 Si(111)-($\sqrt{3} \times \sqrt{3}$)-TlPb

Si(111)-($\sqrt{3} \times \sqrt{3}$)-TlPb is made of a single atomic layer of Tl-Pb alloy grown on the Si(111) surface (Fig. 4a, b) [75]. The surface atomic layer consists of a kagome lattice of 1 ML Tl atoms overlaid with a triangular lattice of $1/3$ ML of Pb. The Pb atoms, located at the T_4 sites of the underlying Si surface, fill the empty cores of the Tl kagome lattice, forming a nearly flat layer with the periodicity of ($\sqrt{3} \times \sqrt{3}$). The total crystal structure belongs to plane group p31m (point group C_{3v}). Since both Pb and Tl are heavy elements, a strong Rashba-type spin splitting can be naturally expected. The electronic band structure revealed by ARPES indeed shows such features (Fig. 4c) [75]. The two sets of spin-split FSs have been found around the $\bar{\Gamma}$ point and near the Brillouin zone boundary, and the energy splittings of the inner and outer FSs amount to 250 and 140 meV at maximum, respectively. The inner FSs are close to a circle in shape while the outer FSs are nearly hexagonal. Furthermore, the spin polarizations obtained by ab initio calculations point to the tangent directions on the former, while significantly deviating from them on the latter. Both sets of FSs exhibit sizable out-of-plane spin component in the $\bar{\Gamma}$ – \bar{M} direction where a mirror plane is absent.

Superconducting transition at 2.25 K has been found for Si(111)-($\sqrt{3} \times \sqrt{3}$)-TlPb through electron transport

measurements [31], which has made this system the first surface atomic-layer superconductors with Rashba-type SOC. The Ginzburg-Landau (GL) coherence length at $T=0$, $\xi_{GL}(0)$, was estimated to be ~ 22 nm from the temperature dependence of out-of-plane upper critical magnetic field, $H_{c2\perp}(T)$. The well-characterized crystal-line and electronic structures, a large Rashba-type spin splitting, and relatively high T_c make this system one of ideal candidates for investigating the effects of Rashba-type SOC on superconductivity.

3.3 Si(111)-($\sqrt{7} \times \sqrt{3}$)-In

This surface structure has been known for a long time [76] and attracted attentions because of their metallic free-electron-like character revealed by ARPES measurements [77]. The same study also found a large electron-phonon coupling, which suggests the possibility of a superconducting transition. Following the finding of superconducting energy gap formation at $T = 3.18$ K using STM [11], its superconducting transition was directly observed through electron transport measurement [12]. This has made this system one of the first 2D superconductors with atomic-scale thickness and well-defined crystal structures. The surface structure can be viewed as double atomic layer of In (corresponding to one unit cell of In(001) planes) deformed to have covalent bondings with the Si(111) surface, resulting in the periodicity of ($\sqrt{7} \times \sqrt{3}$) (see Fig. 5a, b) [78–80]. The nominal coverage of In is 2.4 ML. While the In layers have a pseudo-four-fold symmetry, the total crystal structure including the Si substrate has the C_{1h} symmetry with a mirror plane along the $[11\bar{2}]$ direction.

Very recent ARPES/SARPES measurements and ab initio calculations have revealed that the FS of Si(111)-($\sqrt{7} \times \sqrt{3}$)-In is spin-split due to the SOC (Fig. 5c, d) [32, 81]. The splitting energy at the FS centers around 15–20 meV, but it amounts to ~ 100 meV in some of the regions. The spins are polarized in the momentum space to the tangential directions on the “arc” region of the FS, being consistent with Rashba-type SOC. By sharp contrast, in the “butterfly” region of the FS, the spins point nearly perpendicularly to the Fermi contours. They abruptly change their directions when passing through the $\bar{\Gamma}$ – \bar{X} line, as required by the mirror symmetry regarding the $\bar{\Gamma}$ – \bar{Y} line and the time-reversal symmetry. This unique spin structure can be beautifully explained by the orbital angular momentum (OAM)-based picture [27, 52]; the OAM is stabilized by the coupling between the OAM-induced electric dipole moment and the electric field in the out-of-plane direction, which in turn determines the spin direction through atomistic SOC. Nevertheless, the spin directions are confined in the in-plane except the crossing points on the $\bar{\Gamma}$ – \bar{X} line. In this

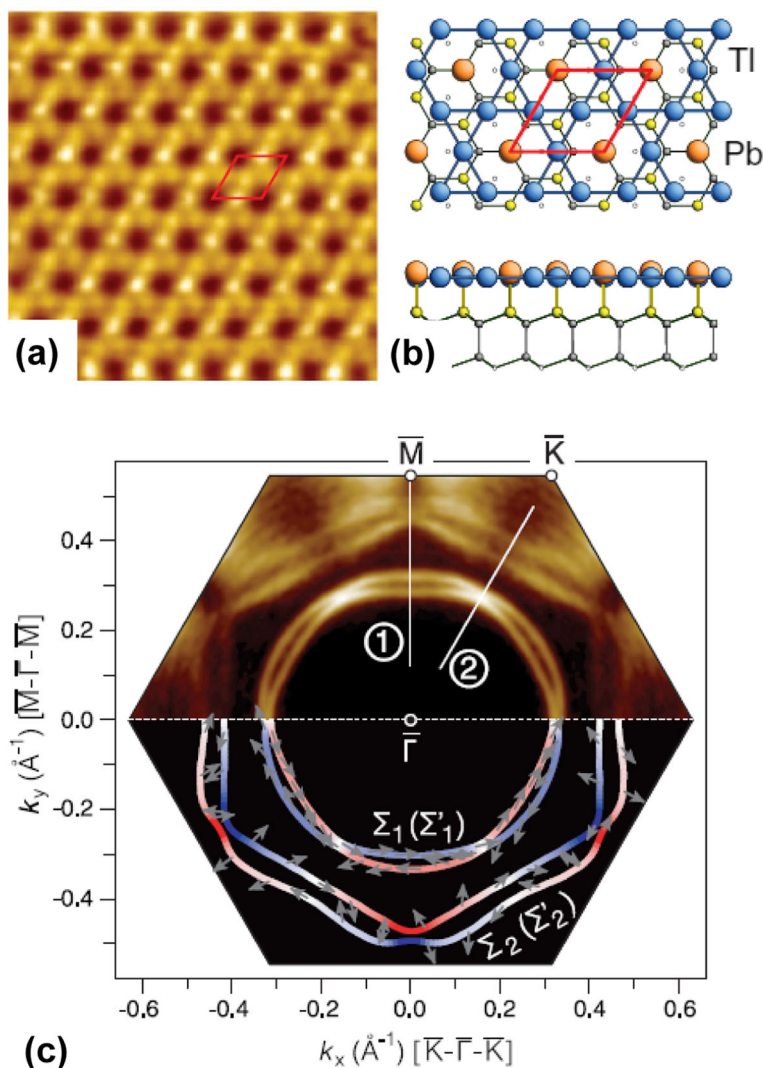


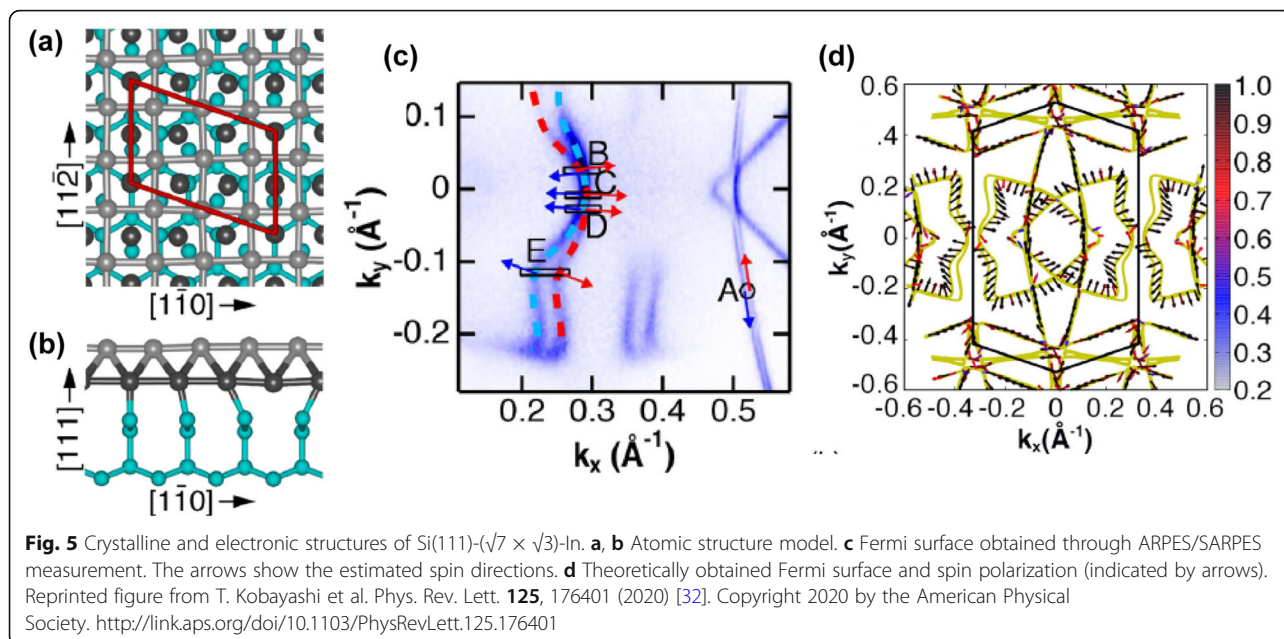
Fig. 4 Crystalline and electronic structures of Si(111)-($\sqrt{3} \times \sqrt{3}$)-TlPb. **a** High-resolution ($5 \times 5 \text{ nm}^2$) STM image. **b** Atomic structure model. **c** Fermi surface obtained through ARPES measurement (upper panel) and ab initio calculations (lower panel). Reprinted figure with permission from A. V. Matetskiy et al. *Phys. Rev. Lett.* **115**, 147003 (2015) [31]. Copyright 2015 by the American Physical Society. <http://link.aps.org/doi/10.1103/PhysRevLett.115.147003>

sense, the spin splitting in this surface may be categorized as a Rashba-type. This fact has important implications in terms of the nature of superconductivity under strong in-plane magnetic fields (see Section 4.2).

The superconducting properties of this surface structure have been well studied by means of electron transport and STM measurements [11–13, 16, 19, 81, 82]. The GL coherence length $\xi_{\text{GL}}(0)$ is estimated to be 25–50 nm [13, 16, 81]. Interestingly, Josephson vortices trapped at atomic steps were observed with STM [16]. This offers clear evidence that an atomic step works as a Josephson junction, reflecting the fact that supercurrents run only through the surface In layers.

3.4 Si(111)-SIC-Pb

Si(111)-SIC-Pb is made of a single Pb atomic layer on Si(111) with a nominal coverage of $\sim 4/3$ ML, which is routinely observed as a Pb-covered Si(111) surface (SIC stands for “striped incommensurate”) [83, 84]. It is a superstructure consisting of two kinds of Si(111)-($\sqrt{3} \times \sqrt{3}$)-Pb phases with different adsorption geometries: one with the center Pb atom of a tetramer located at the H_3 site and the other at the T_4 site, separated by quasi- $(\sqrt{7} \times \sqrt{3})$ domain walls (Fig. 6a–c) [85, 86]. The $(\sqrt{3} \times \sqrt{3})$ phase with the H_3 site is identical to Ge(111)- $\beta(\sqrt{3} \times \sqrt{3})$ -Pb when Si is replaced with Ge. Since the two phases with H_3 and T_4 geometries are very close in



energy, both appear in Si(111)-SIC-Pb as narrow domains. The local symmetry within each domain is C_{3v} (plane group p31m), but the formation of the superstructure lowers the whole symmetry to C_1 .

Ab initio calculations of electronic and spin structures predict large Rashba-type spin splittings for both local phases, which are very similar to those of Ge(111)- $\beta(\sqrt{3} \times \sqrt{3})$ -Pb [71]. However, because of coexistence of the two phases, the band structures acquired through ARPES measurements have broad line widths and hence show no clear splitting (Fig. 6d) [86]. Nevertheless, quantitative model-based analysis on the assumption of the C_{3v} symmetry demonstrates a Rashba-type chiral spin structure for the FS around the $\bar{\Gamma}$ point. The out-of-plane spin components have also been confirmed, constituting a significant portion of the total spin as seen for Ge(111)- $\beta(\sqrt{3} \times \sqrt{3})$ -Pb. These observations are in good agreement with a theoretical prediction [71].

Superconducting transition of Si(111)-SIC-Pb with $T_c = 1.83$ K was discovered first with STM spectroscopy and was confirmed later by electron transport measurement [11, 13]. The GL coherence length $\xi_{GL}(0)$ was estimated to be 49 nm and 74 nm from vortex core size and out-of-plane critical magnetic field, respectively. These have made this system one of the first surface atomic-layer superconductors on a semiconductor. Even above T_c , superconductivity can be induced by the proximity effect if Pb islands are formed on the surface. Enhancement of superconducting energy gap due to geometric confinement by islands or atomic steps have been reported, revealing the effects of the multiple Andreev reflections on a surface 2D system [18, 87].

3.5 Other systems

Si(111)-($\sqrt{7} \times \sqrt{3}$)-Pb is another kind of Pb-covered Si(111) surface structure with the nominal coverage of Pb equal to 6/5 ML [85, 88, 89]. This makes Pb on this surface slightly less packed compared to Si(111)-SIC-Pb. It exhibits a superconducting transition at $T = 1.52$ K, which was revealed through STM measurement [11]. A following STM study revealed anomalous superconducting gap structure, as will be discussed in Section 4.1 [14]. No electron transport measurement or direct observation of Rashba-type spin splitting has been reported so far.

Ge(111)-($\sqrt{3} \times \sqrt{3}$)-TlPb, Ge(111)-(3 \times 3)-TlPb, and Si(111)-(4 \times 4)-TlPb belong to the same family of surface atomic-layer alloys as Si(111)-($\sqrt{3} \times \sqrt{3}$)-TlPb. The basis for these structures is Si(111)-(1 \times 1)-Tl or Ge(111)-(1 \times 1)-Tl surface [55, 56], onto which sub-ML Pb atoms are additionally deposited to form the target structure. They all have strong Rashba-type spin splittings and exhibit superconductivity at low temperatures: $T_c = 2.03, 0.83, 0.79$ K for Ge(111)-($\sqrt{3} \times \sqrt{3}$)-TlPb, Ge(111)-(3 \times 3)-TlPb, and Si(111)-(4 \times 4)-TlPb, respectively [90]. It is worth noting that Si(111)-($\sqrt{3} \times \sqrt{3}$) R30 $^\circ$ -Sn was recently found to exhibit superconductivity with $T_c = 4.7$ K [91]. This system consists of a triangular lattice of Sn atoms on a Si(111) surface with a nominal coverage of only 1/3 ML [92]. While it is intrinsically an antiferromagnetic Mott insulator, it becomes superconducting by hole doping using a heavily doped p-type substrate. Considering the relatively strong SOC of Sn, it may also exhibit Rashba-type spin splitting in its Mott-Hubbard bands.

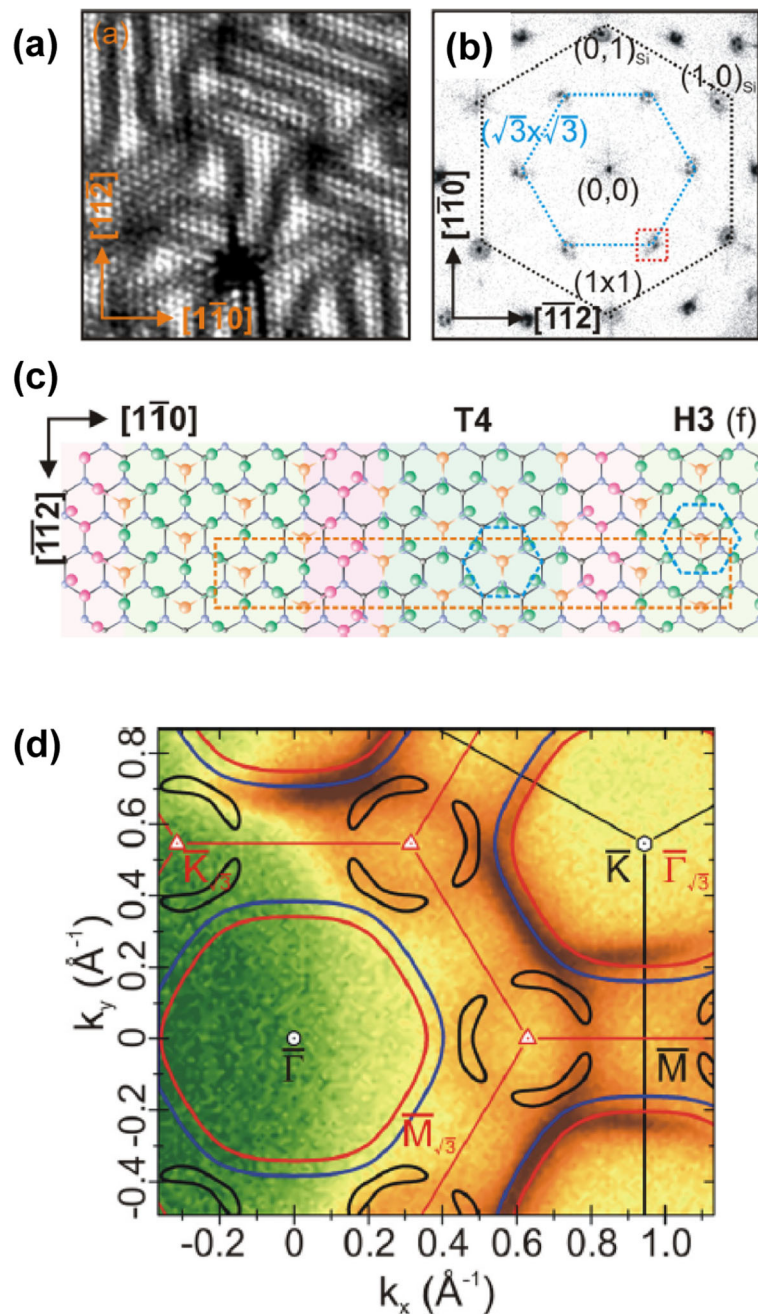


Fig. 6 Crystalline and electronic structures of Si(111)-SiC-Pb. **a** Large-scale STM image (20 nm \times 20 nm). **b** High-resolution LEED pattern with $E = 80$ eV. **c** Schematic structure model for a superstructure with $(\sqrt{3} \times \sqrt{3})$ reconstructions in H_3 and T_4 geometries. **d** Constant-energy contours taken through ARPES 178 meV below E_F and those deduced from a modeling (red and blue lines). Reprinted figure with permission from C. Brand et al. Phys. Rev. B **96**, 035432 (2017) [86]. Copyright 2017 by the American Physical Society. <https://link.aps.org/doi/10.1103/PhysRevB.96.035432>

Finally, we briefly mention quench-condensed atomic-layer films, which are formed by evaporating metal on a liquid-He cooled insulating substrate [1, 93–95]. The fabricated metal films are believed to be strongly disordered (or amorphous) microscopically but homogeneous over mesoscopic/macroscopic scales. Since the prepared

sample must be kept at low temperatures to avoid thermal diffusion and clustering of metal atoms, the morphology and crystallinity of these films are not well characterized. This sample fabrication technique, capable of fine tuning of the film coverage, has widely been used for studies on the superconductor-insulator

transition in 2D systems [93–95]. Recently, quench-condensed Pb and In layers on in situ cleaved GaAs(110) substrates were found to exhibit superconductivity around 2–3 K at a nominal coverage of 1 ML [96, 97]. The persistent superconductivity in this coverage regime, when compared to preceding experiments, may be attributable to the usage of in situ cleaved GaAs(110) as a substrate and to an improved film crystallinity. As in the case of crystalline atomic layers described above, this system may also have Rashba-type SOC due to the inversion symmetry breaking on the surface, but its presence has not been confirmed directly. Multilayer films consisting of Pb and Sb monolayers on Ga(110) have also been reported recently [98], which will be discussed in Section 4.3.

4 Experimental studies on surface atomic-layer superconductors with Rashba/Zeman-type SOC

4.1 Anomalous gap structures and possible singlet-triplet mixing

Recently, Si(111)-($\sqrt{3} \times \sqrt{3}$)-TlPb was studied with STM at low temperatures by Nakamura et al. [99]. The result revealed many surprising anomalous features, which cannot be explained within the framework of the standard BCS theory. The evolution of the characteristic dip structure in dI/dV spectra gives a transition temperature $T_c = 3.1$ K, which is higher than the transport measurement result of $T_c = 2.25$ K. The superconducting energy gap 2Δ is estimated to be 2.3 meV from the separation of the coherence peaks. The gap- T_c ratio $2\Delta/k_B T_c = 8.6$ is much larger than the BCS value 3.52 and $2\Delta/k_B T_c = 4.12 - 4.4$ for Si(111)-($\sqrt{7} \times \sqrt{3}$)-In, Si(111)-SiC-Pb, and Si(111)-($\sqrt{7} \times \sqrt{3}$)-Pb [11]. This indicates that the electron-phonon coupling, likely to be responsible for the emergence of superconductivity, is extremely strong. Furthermore, the observed gap structure is anomalous (Fig. 7a). The overall spectral shape acquired at $T = 0.4$ K is close to a V-shape rather than a U-shape, suggesting the symmetry of Cooper pairs is not of the simple s-wave. This makes a clear contrast to the s-wave-like dI/dV spectra of Si(111)-($\sqrt{7} \times \sqrt{3}$)-In [16]. The spectra of Si(111)-($\sqrt{3} \times \sqrt{3}$)-TlPb cannot be fit with a single gap function such as $\Delta(\mathbf{k}) = \Delta_0$ (s-wave) or $\Delta(\mathbf{k}) = \Delta_1 \cos \phi_k$ (p-wave), where ϕ_k is the azimuthal angle of the momentum \mathbf{k} . The best fitting was obtained with an anisotropic nodeless gap function $\Delta(\mathbf{k})^2 = \Delta_0^2 + \Delta_1^2 \cos^2 \phi_k$. The Δ_0 and Δ_1 values obtained from the fitting analysis show different temperature dependences; Δ_0 disappears at $T = 2.6$ K while Δ_1 persists at the same temperature. These anomalous behaviors are consistent with the presence of two Fermi surfaces (Fig. 4c) and a scenario of weakly interacting two-band superconductivity. They all suggest the possibility of emergence of unconventional superconductivity in this system.

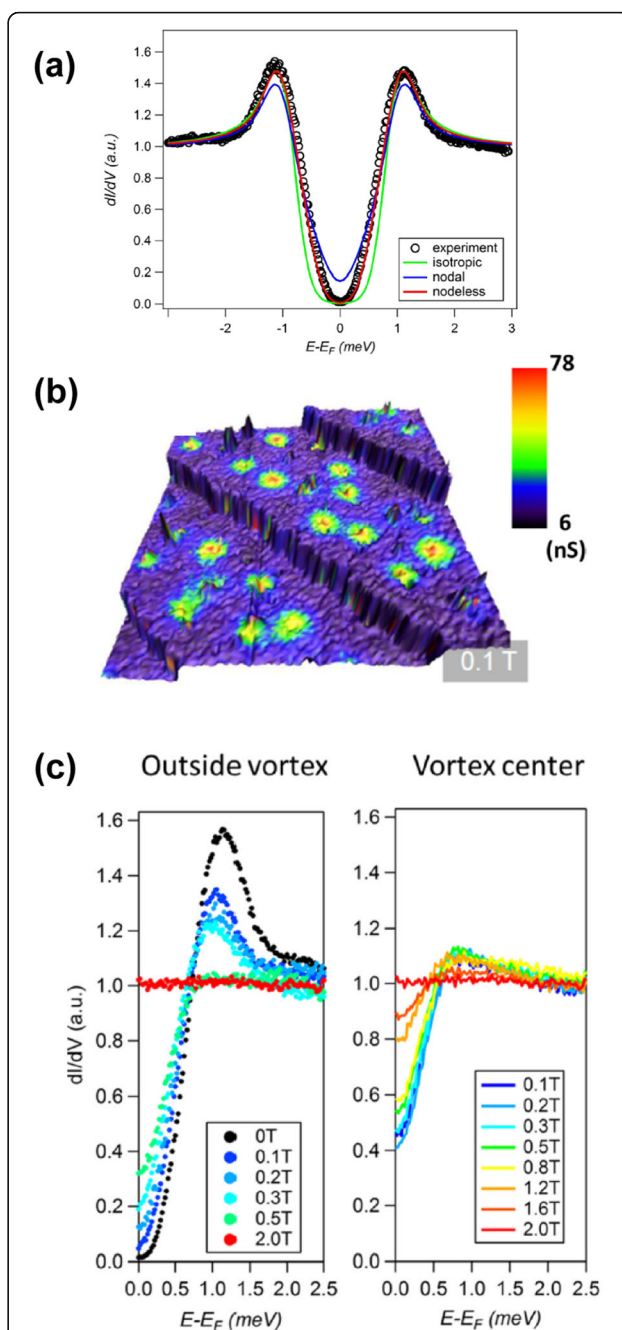


Fig. 7 STM measurements taken for Si(111)-($\sqrt{3} \times \sqrt{3}$)-TlPb. **a** dI/dV spectra taken at $T < 0.5$ K and fitting results with three kinds of gap functions (isotropic, nodal, and nodeless gap functions). **b** The zero bias dI/dV mappings (color code) superimposed on the topographic images (height) obtained at $B = 0.1$ T (scan area $1 \mu\text{m} \times 1 \mu\text{m}$). **c** The dI/dV spectra acquired outside vortices (left) and at the vortex center (right) under different magnetic fields. Reprinted figure with permission from T. Nakamura et al. Phys. Rev. B **98**, 134505 (2018) [99]. Copyright 2018 by the American Physical Society. <https://linkaps.org/doi/10.1103/PhysRevB.98.134505>

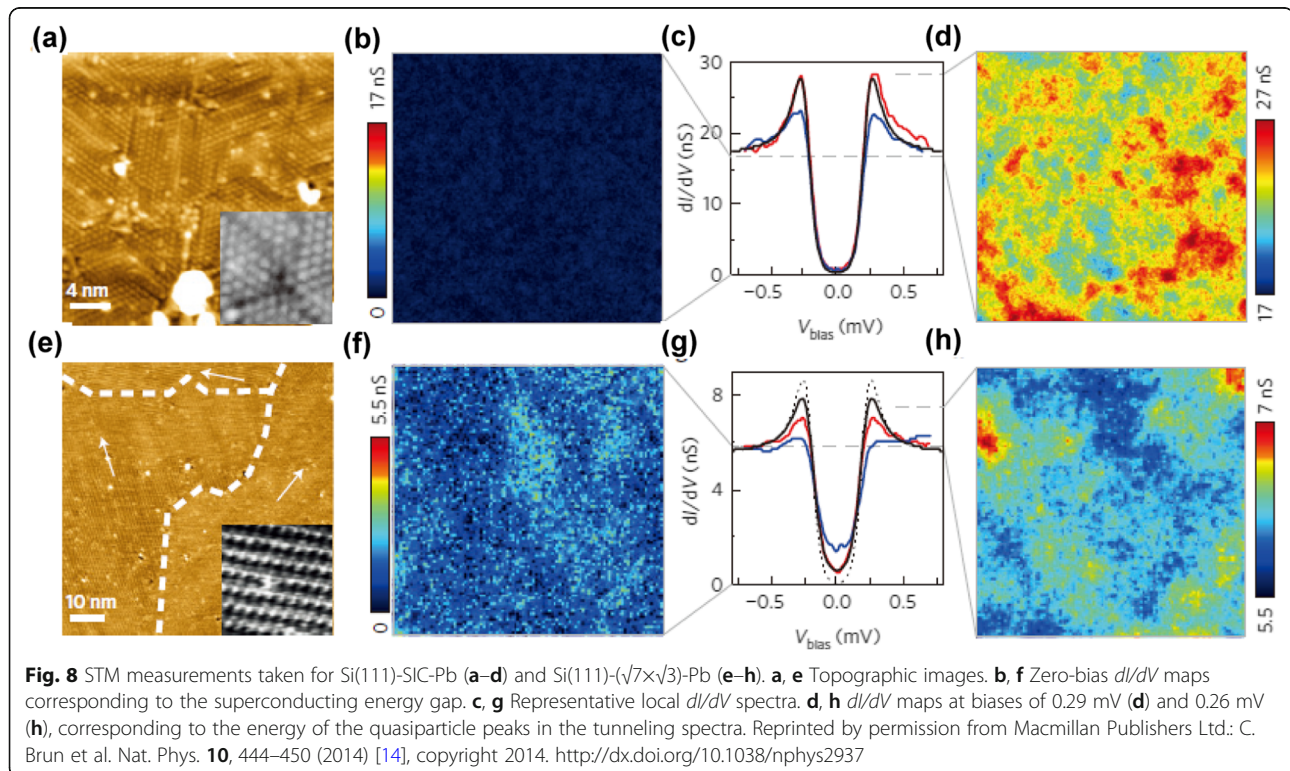
Vortices observed under application of magnetic fields were not uniform in shape and size (Fig. 7b). More surprisingly, the V-shape-like gap structure around the zero bias was found to persist at the center of the vortex core (Fig. 7c). For a conventional vortex, the superconducting order parameter is completely suppressed at its center as was observed for Si(111)-($\sqrt{7} \times \sqrt{3}$)-In [16]. This dip structure continues to exist even when magnetic field is increased above 0.8 T where vortices fully cover the whole surface. At this field, superconductivity must disappear according to the electron transport measurements [31]. In this sense, the dip structure may be called a “pseudo gap”. Two possible mechanisms for this anomaly were discussed. First, application of a strong magnetic field may make Cooper pairs incoherent without destroying them on the mean-field level. This should lead to the disappearance of zero-resistance, but may allow for the gap structure to persist [100]. Second, if the spin-triplet mixing is realized due to Rashba-type SOC as discussed in Section 2.2.1, the order parameters do not necessarily become zero at the vortex center due to the spin degree of freedom [101]. This allows for the existence of so-called “coreless vortex”. More detailed STM studies will be highly desirable to clarify these issues.

Different types of anomaly in the gap structure were also reported for Si(111)-SIC-Pb and Si(111)-($\sqrt{7} \times \sqrt{3}$)-Pb by Brun et al. [14]. Figure 8a–d shows local dI/dV spectra and its spatial mapping acquired for Si(111)-SIC-

Pb at $T = 0.32$ K. While dI/dV spectra at some points can be well reproduced by the standard BCS theory, there exist areas where the coherence peaks at the gap edges are clearly suppressed but the subgap region remains unchanged. The deviation from the conventional behavior was explained by taking into account a non-BCS electron-electron interaction and the resulting admixture of quasi-particle states via virtual processes. For Si(111)-($\sqrt{7} \times \sqrt{3}$)-Pb, the deviation from the standard feature is even more significant (Fig. 8e–h); the coherence peaks are further suppressed and the subgap region becomes partially filled. Phenomenologically, this anomaly can be explained by considering the pair-breaking due to electron-electron collisions [102], but its microscopic origin is not clear. The authors interpreted it in terms of Rashba-type SOC arising from the inversion symmetry breaking in this system. Namely, Rashba-type SOC induces singlet-triplet mixing in Cooper pairs, and the significant momentum dependence of the triplet gap leads to a depairing caused by non-magnetic impurities. The difference between Si(111)-SIC-Pb and Si(111)-($\sqrt{7} \times \sqrt{3}$)-Pb may be attributed to different strengths of Rashba-type SOC in these surfaces.

4.2 Anomalous enhancement of in-plane critical magnetic field

As explained in Section 2.2.2, the spin-momentum locking in the Rashba/Zeeman-type spin-split electronic



bands can enhance the in-plane upper critical field $H_{c2\parallel}$ of a 2D superconductor. Representative results of this effect can be found for MoS₂ and NbSe₂ monolayers with Zeeman-type SOC [6, 60, 61]. When reduced in thickness to a monolayer, these 2D materials exhibit Zeeman-type spin splittings at the \bar{K} and \bar{K}' points (see Section 2.1). Fermi pockets are formed around these points either intrinsically or by electron doping, and superconductivity emerges around 7–10 K [103]. Since Cooper pairs consist of electrons located at \bar{K} and \bar{K}' points where the spins are locked in the out-of-plane direction, Pauli paramagnetism is absent for in-plane magnetic fields. The critical magnetic field along this direction $H_{c2\parallel}$ was found to reach 4–6 times the Pauli limit, which was attributed to the spin-momentum locking.

Recently, the effect of Zeeman-type SOC on the critical magnetic field was revealed by Liu et al. for 4–6-ML-thick Pb ultrathin films grown on Si(111)-SIC-Pb (Fig. 9a) [104]⁵. As described in Section 3.4, the in-plane inversion-symmetry is broken for Si(111)-SIC-Pb. More specifically, the locations of the three Pb atoms within a unit cell are shifted by $\sim 20\%$ compared to those of an ideal Pb(111) plane due to the formation of chemical bondings with the Si substrate (Fig. 9b). When Pb is grown on the surface up to several ML, the lattice distortion extends to the neighboring layers and breaks the in-plane inversion symmetry of the whole Pb film. Ab initio calculations demonstrated the presence of such distortions and Zeeman-type spin splittings of 5–50 meV at the Fermi surface. Superconducting transitions of these ultrathin films were investigated through transport measurements under strong magnetic field up to 47 T (Fig. 9c). The in-plane critical field $H_{c2\parallel}$ was found to reach nearly 3 times the Pauli limit H_p at $T \sim 0.3T_c$ ($T_c = 5.78$ K). It is widely known that the presence of strong atomistic SOC of Pb and elastic scatterings due to non-magnetic impurities can induce frequent spin flippings and suppress the paramagnetic pair-breaking effect [105–107]. However, a prediction by the Klemm-Luther-Beasley theory including this effect significantly deviates from the experimentally obtained $H_{c2\parallel}$ - T curve. By contrast, an analysis based on the spin-momentum locking due to Rashba- and Zeeman-type SOC can reproduce the data better. The effective strengths of the SOC of a 6-ML-thick Pb film were found to be $\tilde{\alpha}_R k_F = 0.22$ meV for Rashba-type and $\tilde{\beta} = 3.16$ meV for Zeeman-type respectively, which are consistent with the ab initio calculations. The result

shows that the Zeeman-type splitting plays a major role in the enhancement of $H_{c2\parallel}$.

Interestingly, Nam et al. also reported strongly enhanced $H_{c2\parallel}$ surpassing the Pauli limit for 5–13-ML-thick Pb films grown on Si(111)-($\sqrt{7} \times \sqrt{3}$)-Pb surfaces [108]. They attributed their finding not to the spin-momentum locking described above, but to dynamic processes originating from it by assuming the presence of Rashba-type SOC. Since Rashba-type SOC leads to in-plane spin polarizations that are locked to electron momentums \mathbf{k} , the spin should flip at every elastic scattering by non-magnetic impurities that accompanies a momentum change (Fig. 10a–c). The spin flipping can also be induced by atomistic SOC, but in this case, the effect is much weaker and the spin flipping time τ_{sf} is by far longer than the elastic scattering time τ_{el} [109, 110]⁶. By contrast, $\tau_{sf} \cong \tau_{el}$ is expected for Rashba-type SOC and thus the spin flipping should be every effective. Nevertheless, since the observed $H_{c2\parallel}$ was governed by the orbital pair-breaking effect in their experiment, direct evidence for this scenario was not obtained.

Very recently, Yoshizawa et al. clarified the effect of dynamic processes considered above using a different atomic-layer system Si(111)-($\sqrt{7} \times \sqrt{3}$)-In [81]. As described in Section 3.3, this surface structure features clear spin splittings that amounts to 15–100 meV on the Fermi surface. While the spin polarization directions strongly deviate from those of the standard Rashba-type SOC, they are still confined within the in-plane directions. Since the out-of-plane component of spin is minimal, the contribution from Zeeman-type SOC is negligible. In this case, the in-plane critical field $H_{c2\parallel}$ might be enhanced by the spin-momentum locking due to Rashba-type SOC, but $H_{c2\parallel}$ should be limited to $\sqrt{2}$ times the Pauli limit H_p (see Section 2.2.2). The experimentally obtained value of $H_{c2\parallel}/H_p$, in contrast, surpasses $\sqrt{2}$ and reaches ~ 3 at $T = 0$ (Fig. 10d–f). This anomalous enhancement of $H_{c2\parallel}$ is fully consistent with the fact that the paramagnetic pair-breaking effect is strongly suppressed by extremely short spin flipping time τ_{sf} . The experimentally obtained relation $\tau_{sf} \cong \tau_{el}$ demonstrates that the dynamic spin-flipping process originating from spin-momentum locking is the primary mechanism for the enhancement of $H_{c2\parallel}$. This effect was referred to as *dynamic* spin-momentum locking in Ref. [81]. It should be contrasted to the *static* effect of spin-momentum locking, which was described above for MoS₂ and NbSe₂ monolayers [6, 60, 61] and Pb ultrathin films on Si(111)-SIC-Pb [104].

⁵In this work and Ref. [81], the term Zeeman-type SOC is used to mean that the spin polarization is in the out-of-plane direction, without referring to the band structure at the \bar{K}/\bar{K}' point.

⁶Conventionally, the spin flipping due to atomistic SOC is called spin-orbit scattering, and τ_{sf} is denoted as τ_{so} . It should be distinguished from the spin flipping due to the Rashba-type SOC discussed here.

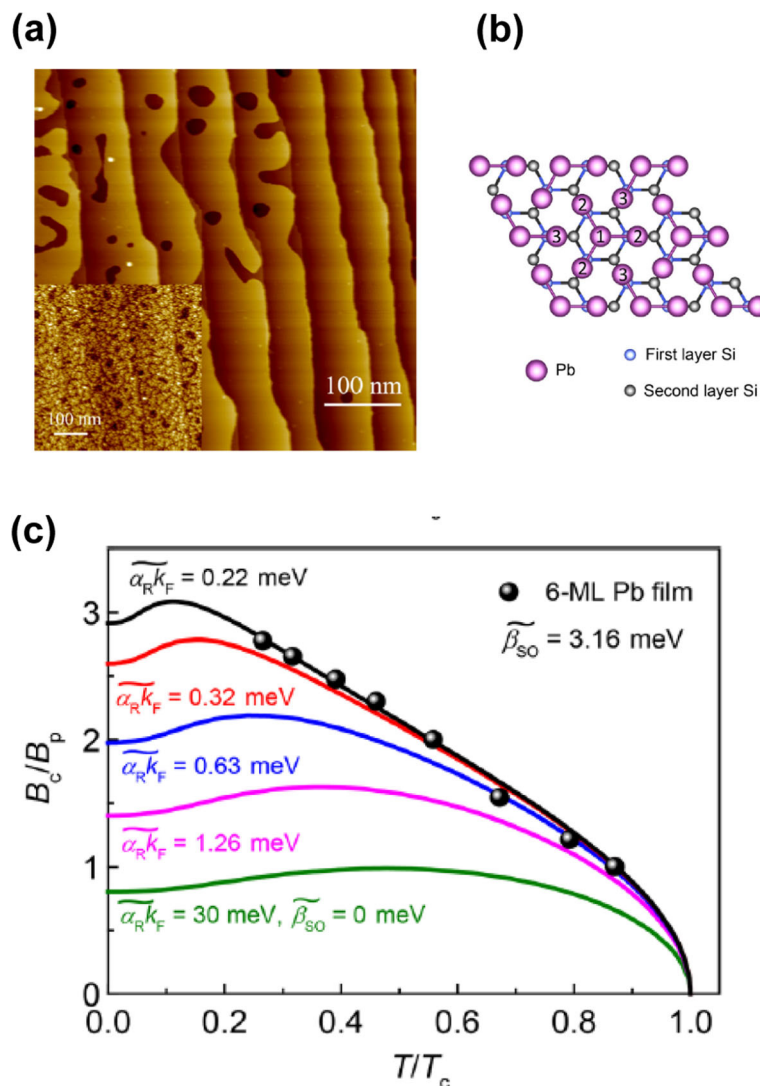


Fig. 9 In-plane critical magnetic field of Pb ultrathin films grown on Si(111)-SiC-Pb. **a** Typical STM image of 4 ML Pb film. **b** Atomic structure model of the substrate surface Si(111)-SiC-Pb. **c** Temperature dependence of in-plane critical field of 6-ML-thick Pb ultrathin films and fitting results based on a theoretical model. Reprinted figure with permission from Y. Liu et al. Phys. Rev. X **8**, 021002 (2018) [104]. Copyright 2018 by the American Physical Society. <https://linkaps.org/doi/10.1103/PhysRevX.8.021002>

4.3 Helical superconducting states

As described in Section 3.5, quench-condensed Pb monolayer films on in situ cleaved GaAs(111) substrates were found to become superconducting around 2–3 K [96, 97]. It was also revealed that the superconductivity is extremely robust against in-plane magnetic fields; the reduction in T_c was found to be only 5–6% even for strong in-plane fields H_{\parallel} exceeding several times the Pauli limit. Considering the possibility of Rashba-type SOC in the present system, this robustness was attributed to the helical superconducting states induced by strong H_{\parallel} (see Section 2.2.3). However, the $H_{c2\parallel}$ enhancement factor due to this effect is in the order of $(\Delta_R/E_F)^2$, where Δ_R is the energy splitting on the FS due to Rashba

SOC and E_F is the Fermi energy [44]. Since $\Delta_R/E_F \ll 1$ for the metal atomic layers on semiconductor substrates found so far, the presence of the helical states is unlikely to explain the observed phenomenon. In the present author's opinion, the result can be well understood in terms of the dynamic spin-flipping process due to the spin-momentum locking as found for Si(111)-($\sqrt{7} \times \sqrt{3}$)-In [81].

Nevertheless, a more convincing signature for the helical states was recently reported by the same group [98]. Masutomi et al. fabricated multilayer films consisting of double or triple Pb monolayers separated by Sb buffer layers on Ga(110) substrates. The sample can be modeled as a 2D superconductor multilayer with a variable

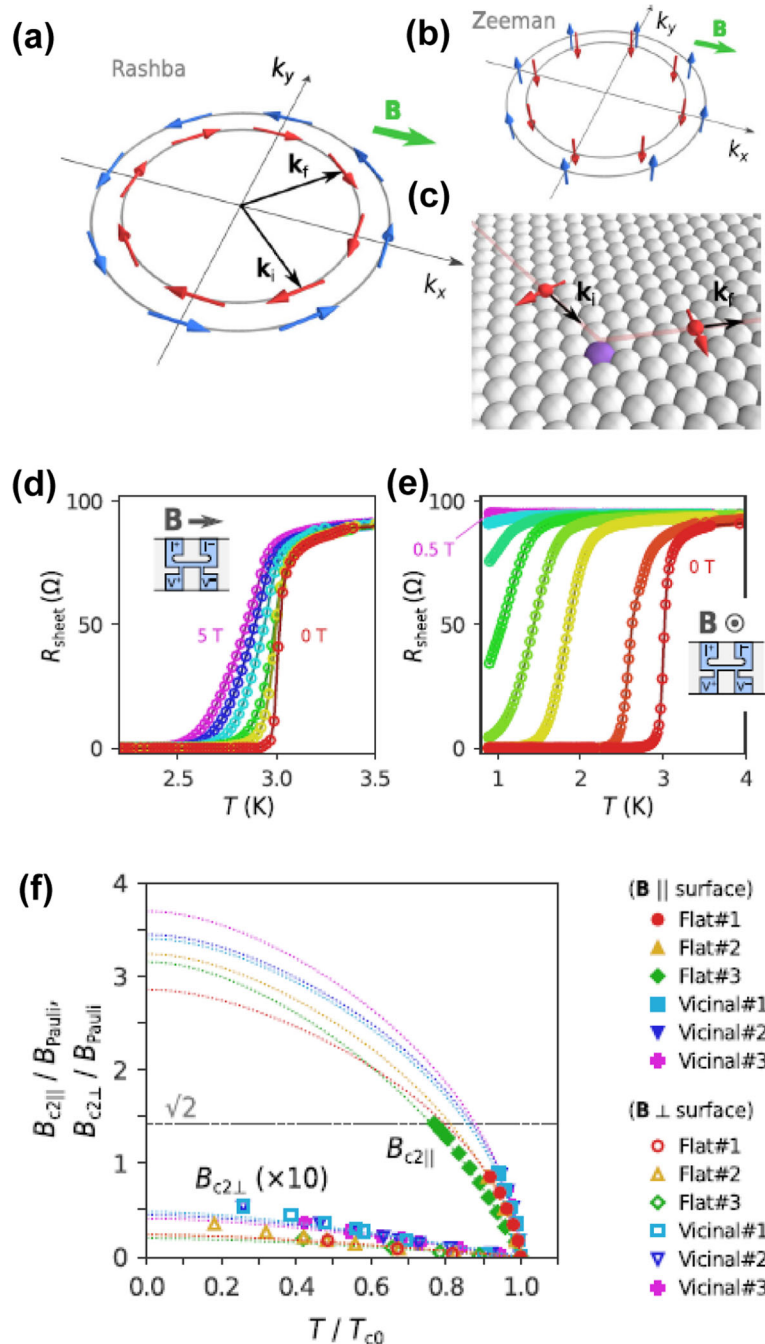


Fig. 10 In-plane critical magnetic field of Si(111)-(√7 × √3)-In. **a** Fermi surface with Rashba-type spin-splitting. **b** Fermi surface with Zeeman-type spin-splitting. **c** Schematic illustration of dynamic process of spin-momentum locking. **d, e** Temperature dependences of sheet resistance for in-plane (**d**) and out-of-plane (**e**) magnetic fields. **f** Temperature dependences of the in-plane and out-of-plane critical magnetic fields normalized with the Pauli limit. Reprinted from Macmillan Publishers Ltd: S. Yoshizawa et al., Nat. Commun. **12**, 1462 (2021) [81]. <http://dx.doi.org/10.1038/s41467-021-21642-1>

interlayer Josephson coupling δ determined by the thickness of the buffer layers (Fig. 11a, b). For $\delta = 0$, since the top and bottom superconducting Pb layers are subject to out-of-plane inversion symmetry breaking in opposite directions, they should have helically modulated order

parameters with $\Delta_1(\mathbf{r}) = \Delta_0 e^{i2\mathbf{q}' \cdot \mathbf{r}}$ and $\Delta_2(\mathbf{r}) = \Delta_0 e^{-i2\mathbf{q}' \cdot \mathbf{r}}$. Here \mathbf{q}' is given by Eq. (13). These modulations are intermixed with the introduction of a finite interlayer coupling ($\delta \neq 0$), leading to $\Delta_1(\mathbf{r}) = \Delta_0 (e^{i2\mathbf{q}' \cdot \mathbf{r}} + \delta e^{-i2\mathbf{q}' \cdot \mathbf{r}})$ and $\Delta_2(\mathbf{r}) = \Delta_0 (e^{-i2\mathbf{q}' \cdot \mathbf{r}} + \delta e^{i2\mathbf{q}' \cdot \mathbf{r}})$. Such unconventional

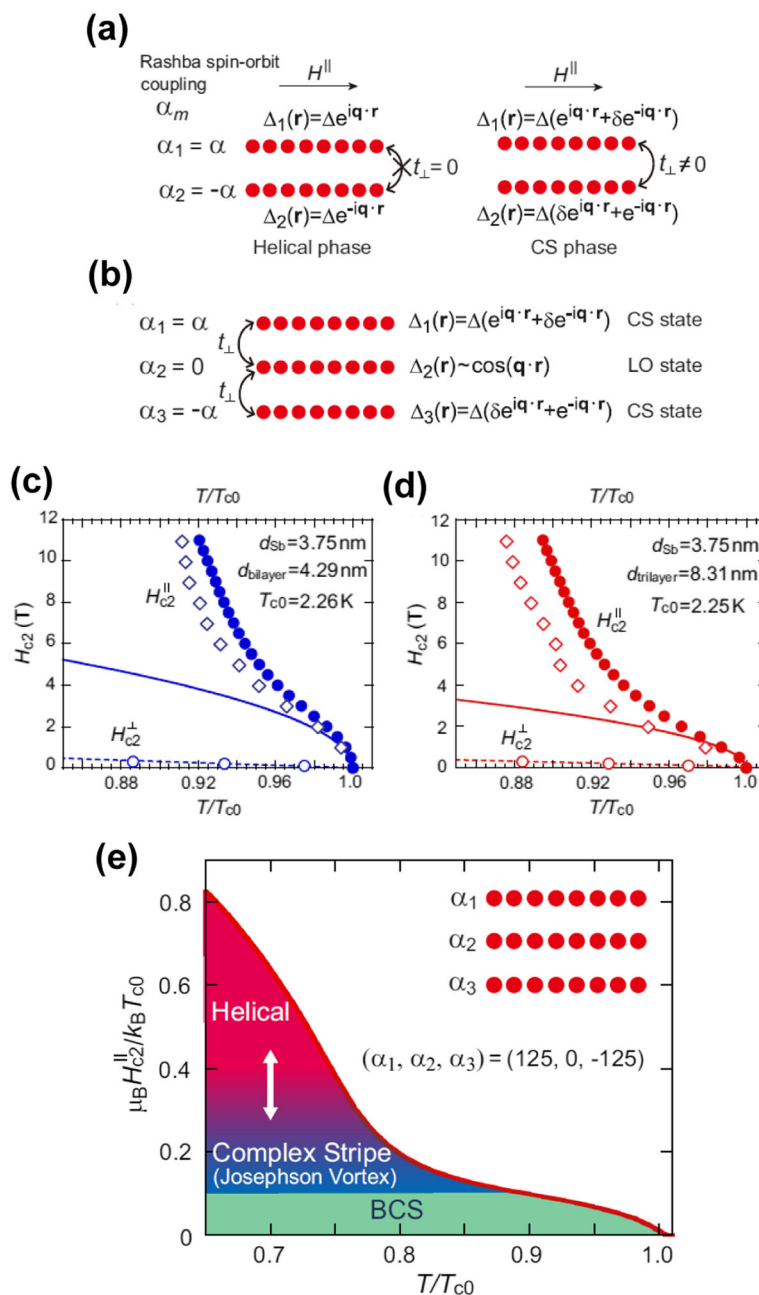


Fig. 11 In-plane critical magnetic field of quench-condensed Pb/Sb multiple layers on in situ cleaved GaAs(111). **a, b** Theoretical models for Pb bilayer **(a)** and Pb trilayer **(b)** systems in an in-plane magnetic field H_{\parallel} . Each Pb layer is separated by a Sb layer. **c, d** Temperature dependences of the in-plane critical magnetic fields for Pb bilayer **(c)** and Pb trilayer **(d)** systems. **e** Theoretical prediction of the phase diagram for a Pb trilayer. Reprinted figure with permission from R. Masutomi et al. Phys. Rev. B 101, 184502 (2020) [98]. Copyright 2020 by the American Physical Society. <https://link.aps.org/doi/10.1103/PhysRevB.101.184502>

superconducting states with phase and amplitude modulations are called a complex stripe (CS) phase [111]. Experimentally, the temperature dependences of $H_{c2\parallel}$ for such multilayers were found to exhibit sharp upturn behaviors at lower temperatures, deviating from the $(1 - T/T_c)^{1/2}$ dependence expected from the Ginzburg-Landau

theory (Fig. 11c, d). The overall temperature dependences are well reproduced by a theoretical model that predicts a BCS-CS-helical phase transition below $\sim 0.8 T_c$ (Fig. 11e). More direct evidence for such spatially modulated superconducting states, e.g., with STM imaging, are highly desirable.

5 Summary and outlook

In the present article, we have reviewed representative surface atomic-layer superconductors that have Rashba/Zeeman-type SOC due to the out-of-plane and in-plane inversion symmetry breakings. The experimental signatures of Rashba/Zeeman-type SOC revealed in superconducting phenomena have already been accumulated. Obviously, however, such studies are still in an early stage and many questions and problems have remained unresolved. Particularly, the anomalies found for Si(111)-($\sqrt{3} \times \sqrt{3}$)-TlPb are very interesting and worthy of further experimental and theoretical investigations. So far, direct evidence for FFLO and helical states is still missing, and experimental verifications of electromagnetic effect such as supercurrent-induced spin polarization and its inverse effect have not been reported. If successful, they are expected to bring a breakthrough in this field.

For this purpose, further instrumentational progress is indispensable. For example, high-resolution STM operating at dilution-refrigerator temperatures will be very helpful to clarify the superconducting gap structures, which is now feasible thanks to the recent remarkable progress in STM instrumentation [112]. Low-temperature STM that operates under a strong in-plane magnetic field may allow one to directly observe spatial modulations of the order parameter. Laser-based ultrahigh-resolution ARPES/SARPES will also play an important role for detecting fine spin-split structures that strongly affect superconducting properties [32, 81, 113]. High-resolution ARPES operating at liquid helium temperatures may directly elucidate the superconducting gap structures in the momentum space [114]. Aside from such spectroscopic tools, electron transport measurement will continue to be central to the researches treated here. Despite its simple concept, actual instrumentation for surface atomic-layer systems is challenging; one needs to integrate the standard surface science techniques with an extreme environment with low-temperatures and high magnetic-fields and to probe the sample without destroying it. Such progress has already been made [31, 81, 82, 115, 116], but apparently, this kind of highly customized machine is very costly. An alternative method would be to put a passivation layer for protecting the chemically active surface, which allows one to take advantage of existing powerful commercial instruments. This has already been realized for ultrathin metal films with several ML thickness [9, 104, 108], but the extension of such a technique to samples with single atomic layers is highly demanded for further developments.

In the field of spintronics and valleytronics, Rashba/Zeeman-type SOC has been used to generate

spin-polarized currents in the real space [30, 35, 62, 117]. This fascinating feature will be enriched further with the introduction of superconductivity as considered here. The 2D system with Rashba-type spin splitting under a Zeeman field is also a candidate for realizing topological superconductivity and Majorana zero-modes, which are being intensively investigated to realize robust quantum computations [57, 118–120]. The studies of surface atomic-layer superconductors described here may also contribute to the development of these fields in the near future.

Acknowledgements

The author thanks K. Sakamoto, K. Yaji, S. Yoshizawa, and A. Tanaka for fruitful discussions and/or critical readings of the manuscript.

Author's contributions

The author contributed to all aspects of the manuscript. The author read and approved the final manuscript.

Author's information

Takashi Uchihashi is the group leader of Surface Quantum Phase Materials Group, International Center for Materials Nanoarchitectonics (WPI-MANA), National Institute for Materials Science (NIMS), Japan.

Funding

The author is financially supported by JSPS KAKENHI Grant No. 20K20904 and by the World Premier International Research Center (WPI) Initiative on Materials Nanoarchitectonics, MEXT, Japan.

Availability of data and materials

All data and figures presented in this article are based on the materials available in public through the corresponding references with their permissions.

Declarations

Ethics approval and consent to participate

Not applicable.

Consent for publication

Not applicable.

Competing interests

The author declares that he has no competing interests.

Received: 30 July 2021 Accepted: 8 November 2021

Published online: 30 November 2021

References

1. T. Uchihashi, *Supercond. Sci. Technol.* **30**, 013002 (2017)
2. Y. Saito, T. Nojima, Y. Iwasa, *Nat Rev Mat* **2**, 16094 (2016)
3. A.T. Bollinger, G. Dubuis, J. Yoon, D. Pavuna, J. Misewich, I. Bozovic, *Nature* **472**, 458–460 (2011)
4. Q.-Y. Wang, Z. Li, W.-H. Zhang, Z.-C. Zhang, J.-S. Zhang, W. Li, H. Ding, Y.-B. Ou, P. Deng, K. Chang, J. Wen, C.-L. Song, K. He, J.-F. Jia, S.-H. Ji, Y.-Y. Wang, L.-L. Wang, X. Chen, X.-C. Ma, Q.-K. Xue, *Chin Phys Lett* **29**, 037402 (2012)
5. Y. Saito, Y. Kasahara, J. Ye, Y. Iwasa, T. Nojima, *Science* **350**, 409–413 (2015)
6. X. Xi, Z. Wang, W. Zhao, J.-H. Park, K.T. Law, H. Berger, L. Forro, J. Shan, K.F. Mak, *Nat Phys* **12**, 139–143 (2016)
7. Y. Cao, V. Fatemi, S. Fang, K. Watanabe, T. Taniguchi, E. Kaxiras, P. Jarillo-Herrero, *Nature* **556**, 43 (2018)
8. Y. Yu, L. Ma, P. Cai, R. Zhong, C. Ye, J. Shen, G.D. Gu, X.H. Chen, Y. Zhang, *Nature* **575**, 156–163 (2019)
9. M.M. Özer, J.R. Thompson, H.H. Weitering, *Nat Phys* **2**, 173–176 (2006)
10. S.Y. Qin, J. Kim, Q. Niu, C.K. Shih, *Science* **324**, 1314–1317 (2009)

11. T. Zhang, P. Cheng, W.J. Li, Y.J. Sun, G. Wang, X.G. Zhu, K. He, L.L. Wang, X.C. Ma, X. Chen, Y.Y. Wang, Y. Liu, H.Q. Lin, J.F. Jia, Q.K. Xue, *Nat Phys* **6**, 104–108 (2010)
12. T. Uchihashi, P. Mishra, M. Aono, T. Nakayama, *Phys Rev Lett* **107**, 207001 (2011)
13. M. Yamada, T. Hirahara, S. Hasegawa, *Phys Rev Lett* **110**, 237001 (2013)
14. C. Brun, T. Cren, V. Cherkez, F. Debontridder, S. Pons, D. Fokin, M.C. Tringides, S. Bozhko, L.B. Ioffe, B.L. Altshuler, D. Roditchev, *Nat Phys* **10**, 444–450 (2014)
15. T. Uchihashi, *AAPPS Bulletin* **27**, 18–25 (2017)
16. S. Yoshizawa, H. Kim, T. Kawakami, Y. Nagai, T. Nakayama, X. Hu, Y. Hasegawa, T. Uchihashi, *Phys Rev Lett* **113**, 247004 (2014)
17. D. Roditchev, C. Brun, L. Serrier-Garcia, J.C. Cuevas, V.H.L. Bessa, M.V. Milosevic, F. Debontridder, V. Stolyarov, T. Cren, *Nat Phys* **11**, 332–337 (2015)
18. H. Kim, S.-Z. Lin, M.J. Graf, Y. Miyata, Y. Nagai, T. Kato, Y. Hasegawa, *Phys Rev Lett* **117**, 116802 (2016)
19. S. Yoshizawa, E. Minamitani, S. Vijayaraghavan, P. Mishra, Y. Takagi, T. Yokoyama, H. Oba, J. Nitta, K. Sakamoto, S. Watanabe, T. Nakayama, T. Uchihashi, *Nano Lett* **17**, 2287–2293 (2017)
20. E.I. Rashba, V.I. Sheka, F.T. Tela, *Collected Papers* **2**, 162–176 (1959)
21. Y.A. Bychkov, E.I. Rashba, *JETP Lett* **39**, 78–81 (1984)
22. J. Nitta, T. Akazaki, H. Takayanagi, T. Enoki, *Phys Rev Lett* **78**, 1335–1338 (1997)
23. S. LaShell, B.A. McDougall, E. Jensen, *Phys Rev Lett* **77**, 3419–3422 (1996)
24. L. Petersen, P. Hedegård, *Surf Sci* **459**, 49–56 (2000)
25. C.R. Ast, J. Henk, A. Ernst, L. Moreschini, M.C. Falub, D. Pacilé, P. Bruno, K. Kern, M. Grioni, *Phys Rev Lett* **98**, 186807 (2007)
26. M. Nagano, A. Kodama, T. Shishidou, and T. Oguchi, *J Phys Condens Matter* **21**, 064239 (2009).
27. S.R. Park, C.H. Kim, J. Yu, J.H. Han, C. Kim, *Phys Rev Lett* **107**, 156803 (2011)
28. K. Yaji, Y. Ohtsubo, S. Hatta, H. Okuyama, K. Miyamoto, T. Okuda, A. Kimura, H. Namatame, M. Taniguchi, T. Aruga, *Nat Commun* **1**, 17 (2010)
29. K. Sakamoto, H. Kakuta, K. Sugawara, K. Miyamoto, A. Kimura, T. Kuzumaki, N. Ueno, E. Annese, J. Fujii, A. Kodama, T. Shishidou, H. Namatame, M. Taniguchi, T. Sato, T. Takahashi, T. Oguchi, *Phys Rev Lett* **103**, 156801 (2009)
30. K. Sakamoto, T.-H. Kim, T. Kuzumaki, B. Müller, Y. Yamamoto, M. Ohtaka, J.R. Osiecki, K. Miyamoto, Y. Takeichi, A. Harasawa, S.D. Stolwijk, A.B. Schmidt, J. Fujii, R.I.G. Uhrberg, M. Donath, H.W. Yeom, T. Oda, *Nat Commun* **4**, 2073 (2013)
31. A.V. Matetskiy, S. Ichinokura, L.V. Bondarenko, A.Y. Tupchaya, D.V. Gruznev, A. V. Zotov, A.A. Saranin, R. Hobar, A. Takayama, S. Hasegawa, *Phys Rev Lett* **115**, 147003 (2015)
32. T. Kobayashi, Y. Nakata, K. Yaji, T. Shishidou, D. Agterberg, S. Yoshizawa, F. Komori, S. Shin, M. Weinert, T. Uchihashi, K. Sakamoto, *Phys Rev Lett* **125**, 176401 (2020)
33. V.M. Edelstein, *J Exp Theor Phys* **68**, 1244 (1989)
34. L.P. Gor'kov, E.I. Rashba, *Phys Rev Lett* **87**, 037004 (2001)
35. V.M. Edelstein, *Phys Rev Lett* **75**, 2004–2007 (1995)
36. S.K. Yip, *Phys Rev B* **65**, 144508 (2002)
37. S. Fujimoto, *Phys Rev B* **72**, 024515 (2005)
38. S. Fujimoto, *J Physical Soc Japan* **76**, 034712 (2007)
39. P. Frigeri, D. Agterberg, A. Koga, M. Sigrist, *Phys Rev Lett* **92**, 097001 (2004)
40. V. Barzykin, L.P. Gor'kov, *Phys Rev Lett* **89**, 227002 (2002)
41. K.V. Samokhin, *Phys Rev B* **70**, 104521 (2004)
42. R.P. Kaur, D.F. Agterberg, M. Sigrist, *Phys Rev Lett* **94**, 137002 (2005)
43. O. Dimitrova, M.V. Feigel'man, *Phys Rev B* **76**, 014522 (2007)
44. M. Houzet, J.S. Meyer, *Phys Rev B* **92**, 014509 (2015)
45. E. Bauer, G. Hilscher, H. Michor, C. Paul, E.W. Scheidt, A. Griбанov, Y. Seropegin, H. Noë, M. Sigrist, P. Rogl, *Phys Rev Lett* **92**, 027003 (2004)
46. T. Akazawa, H. Hidaka, T. Fujiwara, T. C. Kobayashi, E. Yamamoto, Y. Haga, R. Settai, and Y. Nuki, *J. Phys. Condens. Matter* **16**, L29–L32 (2004).
47. N. Kimura, K. Ito, K. Saitoh, Y. Umeda, H. Aoki, T. Terashima, *Phys Rev Lett* **95**, 247004 (2005)
48. E. Bauer, M. Sigrist, *Non-centrosymmetric Superconductors* (Springer, Heidelberg, 2012)
49. M. Smidman, M.B. Salamon, H.Q. Yuan, D.F. Agterberg, *Rep Prog Phys* **80**, 036501 (2017)
50. R.J. Elliott, *Phys Ther Rev* **96**, 280–287 (1954)
51. T. Oguchi and T. Shishidou, *J Phys Condens Matter* **21**, 092001 (2009).
52. S.R. Park, C. Kim, *J Electron Spectros Relat Phenom* **201**, 6–17 (2015)
53. S. Vajna, E. Simon, A. Szilva, K. Palotas, B. Ujfalussy, L. Szunyogh, *Phys Rev B* **85**, 075404 (2012)
54. K. Yaji, A. Visikovsky, T. Iimori, K. Kuroda, S. Hayashi, T. Kajiwara, S. Tanaka, F. Komori, S. Shin, *Phys Rev Lett* **122**, 126403 (2019)
55. S. Hatta, C. Kato, N. Tsuboi, S. Takahashi, H. Okuyama, T. Aruga, A. Harasawa, T. Okuda, T. Kinoshita, *Phys Rev B* **76**, 075427 (2007)
56. K. Sakamoto, T. Oda, A. Kimura, K. Miyamoto, M. Tsujikawa, A. Imai, N. Ueno, H. Namatame, M. Taniguchi, P.E.J. Eriksson, R.I.G. Uhrberg, *Phys Rev Lett* **102**(096805), 096805 (2009)
57. N.F.Q. Yuan, K.F. Mak, K.T. Law, *Phys Rev Lett* **113**, 097001 (2014)
58. D. Xiao, G.-B. Liu, W. Feng, X. Xu, W. Yao, *Phys Rev Lett* **108**, 196802 (2012)
59. H. Yuan, M.S. Bahramy, K. Morimoto, S. Wu, K. Nomura, B.-J. Yang, H. Shimotani, R. Suzuki, M. Toh, C. Kloc, X. Xu, R. Arita, N. Nagaosa, Y. Iwasa, *Nat Phys* **9**, 563–569 (2013)
60. J.M. Lu, O. Zheliuk, I. Leermakers, N.F.Q. Yuan, U. Zeitler, K.T. Law, J.T. Ye, *Science* **350**, 1353–1357 (2015)
61. Y. Saito, Y. Nakamura, M.S. Bahramy, Y. Kohama, J. Ye, Y. Kasahara, Y. Nakagawa, M. Onga, M. Tokunaga, T. Nojima, Y. Yanase, Y. Iwasa, *Nat Phys* **12**, 144–149 (2016)
62. V.M. Edelstein, *Solid State Commun* **73**, 233–235 (1990)
63. S. Fujimoto, *J. Phys. Soc. Jpn.* **76**, 051008 (2007).
64. A.M. Clogston, *Phys Rev Lett* **9**, 266–267 (1962)
65. B.S. Chandrasekhar, *Appl Phys Lett* **1**, 7–8 (1962)
66. D.F. Agterberg, R.P. Kaur, *Phys Rev B* **75**, 064511 (2007)
67. P. Fulde, R.A. Ferrell, *Phys Ther Rev* **135**, A550–A563 (1964)
68. A.I. Larkin, Y. Ovchinnikov, *J Exp Theor Phys* **20**, 762 (1965)
69. S.A. de Vries, P. Goettkindt, P. Steadman, E. Vlieg, *Phys Rev B* **59**, 13301–13308 (1999)
70. K. Yaji, S. Hatta, T. Aruga, H. Okuyama, *Phys Rev B* **86**, 235317 (2012)
71. X.-Y. Ren, H.-J. Kim, S. Yi, Y. Jia, J.-H. Cho, *Phys Rev B* **94**, 075436 (2016)
72. S. Hatta, T. Noma, H. Okuyama, T. Aruga, *Phys Rev B* **90**, 245407 (2014)
73. H. Kim, Y. Miyata, Y. Hasegawa, *Supercond Sci Technol* **29**, 084006 (2016)
74. H. Huang, H. Toyama, L.V. Bondarenko, A.Y. Tupchaya, D.V. Gruznev, A. Takayama, R. Hobar, A. Akiyama, A.V. Zotov, A.A. Saranin, S. Hasegawa, *Supercond. Sci. Technol.* **33**, 075007 (2020)
75. D.V. Gruznev, L.V. Bondarenko, A.V. Matetskiy, A.A. Yakovlev, A.Y. Tupchaya, S. V. Ereemeev, E.V. Chulkov, J.-P. Chou, C.-M. Wei, M.-Y. Lai, Y.-L. Wang, A.V. Zotov, A.A. Saranin, *Sci Rep* **4**, 4742 (2014)
76. J. Kraft, S.L. Surnev, F.P. Netzer, *Surf Sci* **340**, 36–48 (1995)
77. E. Rotenberg, H. Koh, K. Rossnagel, H. Yeom, J. Schäfer, B. Krenzer, M. Rocha, S. Kevan, *Phys Rev Lett* **91**, 246404 (2003)
78. J. Park, M. Kang, *Phys Rev Lett* **109**, 166102 (2012)
79. T. Shirasawa, S. Yoshizawa, T. Takahashi, T. Uchihashi, *Phys Rev B* **99**, 100502(R) (2019)
80. K. Uchida, A. Oshiyama, *Phys Rev B* **87**, 165433 (2013)
81. S. Yoshizawa, T. Kobayashi, Y. Nakata, K. Yaji, K. Yokota, F. Komori, S. Shin, K. Sakamoto, T. Uchihashi, *Nat Commun* **12**, 1462 (2021)
82. Y. Wu, M.-C. Duan, N. Liu, G. Yao, D. Guan, S. Wang, Y.-Y. Li, H. Zheng, C. Liu, J.-F. Jia, *Phys Rev B* **99**, 140506 (2019)
83. L. Seehofer, G. Falkenberg, D. Daboul, R.L. Johnson, *Phys Rev B* **51**, 13503–13515 (1995)
84. K. Horikoshi, X. Tong, T. Nagao, S. Hasegawa, *Phys Rev B* **60**, 13287–13290 (1999)
85. T.-L. Chan, C.Z. Wang, M. Hupalo, M.C. Tringides, Z.-Y. Lu, K.M. Ho, *Phys Rev B* **68**, 045410 (2003)
86. C. Brand, S. Muff, M. Fanciulli, H. Pfñür, M.C. Tringides, J.H. Dil, C. Tegenkamp, *Phys Rev B* **96**, 035432 (2017)
87. J. Kim, V. Chua, G.A. Fiete, H. Nam, A.H. MacDonald, C.K. Shih, *Nat Phys* **8**, 463–468 (2012)
88. W.H. Choi, H. Koh, E. Rotenberg, H.W. Yeom, *Phys Rev B* **75**, 075329 (2007)
89. S. Brochard, E. Artacho, O. Custance, I. Brihuega, A.M. Baró, J.M. Soler, J.M. Gómez-Rodríguez, *Phys Rev B* **66**, 205403 (2002)
90. T. Nakamura, A. Takayama, R. Hobar, D.V. Gruznev, A.V. Zotov, A.A. Saranin, S. Hasegawa, *Appl Surf Sci* **479**, 679–684 (2019)
91. X. Wu, F. Ming, T.S. Smith, G. Liu, F. Ye, K. Wang, S. Johnston, H.H. Weitering, *Phys Rev Lett* **125**, 117001 (2020)
92. F. Ming, S. Johnston, D. Mulugeta, T.S. Smith, P. Vilmercati, G. Lee, T.A. Maier, P.C. Snijders, H.H. Weitering, *Phys Rev Lett* **119**, 266802 (2017)
93. M. Strongin, R.S. Thompson, O.F. Kammerer, J.E. Crow, *Phys Rev B* **1**, 1078–1091 (1970)
94. A.M. Goldman, N. Markovic, *Phys Today* **51**, 39–44 (1998)

95. D.B. Haviland, Y. Liu, A.M. Goldman, *Phys Rev Lett* **62**, 2180–2183 (1989)
96. T. Sekihara, R. Masutomi, T. Okamoto, *Phys Rev Lett* **111**, 057005 (2013)
97. T. Sekihara, T. Miyake, R. Masutomi, T. Okamoto, *J Physical Soc Japan* **84**, 064710 (2015)
98. R. Masutomi, T. Okamoto, Y. Yanase, *Phys Rev B* **101**, 184502 (2020)
99. T. Nakamura, H. Kim, S. Ichinokura, A. Takayama, A.V. Zotov, A.A. Saranin, Y. Hasegawa, S. Hasegawa, *Phys Rev B* **98**, 134505 (2018)
100. T.I. Baturina, D.R. Islamov, J. Bentner, C. Strunk, M.R. Baklanov, A. Satta, *J Exper Theor Phys Lett* **79**, 337–341 (2004)
101. E. Pechenik, B. Rosenstein, B.Y. Shapiro, I. Shapiro, *Phys Rev B* **65**, 214532 (2002)
102. B.L. Altshuler, A.G. Aronov, D.E. Khmel'nitsky, *J Physics C Solid State Physics* **15**, 7367–7386 (1982)
103. J.T. Ye, Y.J. Zhang, R. Akashi, M.S. Bahramy, R. Arita, Y. Iwasa, *Science* **338**, 1193–1196 (2012)
104. Y. Liu, Z. Wang, X. Zhang, C. Liu, Y. Liu, Z. Zhou, J. Wang, Q. Wang, Y. Liu, C. Xi, M. Tian, H. Liu, J. Feng, X.C. Xie, J. Wang, *Phys Rev X* **8**, 021002 (2018)
105. K. Maki, T. Tsuneto, *ProgTheor Physics* **31**, 945–956 (1964)
106. K. Maki, *Phys Ther Rev* **148**, 362–369 (1966)
107. R.A. Klemm, A. Luther, M.R. Beasley, *Phys Rev B* **12**, 877–891 (1975)
108. H. Nam, H. Chen, T. Liu, J. Kim, C. Zhang, J. Yong, T.R. Lemberger, P.A. Kratz, J.R. Kirtley, K. Moler, P.W. Adams, A.H. MacDonald, C.K. Shih, *Proc Natl Acad Sci U S A* **113**, 10513–10517 (2016)
109. A.A. Abrikosov, L.P. Gor'kov, *J Exp Theor Phys* **15**, 752–757 (1962)
110. R. Meservey, P.M. Tedrow, *Physics Letters A* **58**, 131–132 (1976)
111. T. Watanabe, T. Yoshida, Y. Yanase, *Phys Rev B* **92**, 174502 (2015)
112. T. Machida, Y. Kohsaka, T. Hanaguri, *Rev Sci Instrum* **89**, 093707 (2018)
113. K. Yaji, A. Harasawa, K. Kuroda, S. Toyohisa, M. Nakayama, Y. Ishida, A. Fukushima, S. Watanabe, C. Chen, F. Komori, S. Shin, *Rev Sci Instrum* **87**, 053111 (2016)
114. T. Kiss, T. Shimojima, K. Ishizaka, A. Chainani, T. Togashi, T. Kanai, X.Y. Wang, C.T. Chen, S. Watanabe, S. Shin, *Rev Sci Instrum* **79**, 023106 (2008)
115. H. Nam, P.H. Su, C.K. Shih, *Rev Sci Instrum* **89**, 043901 (2018)
116. M.-C. Duan, Z.-L. Liu, J.-F. Ge, Z.-J. Tang, G.-Y. Wang, Z.-X. Wang, D. Guan, Y.-Y. Li, D. Qian, C. Liu, J.-F. Jia, *Rev Sci Instrum* **88**, 073902 (2017)
117. A. Soumyanarayanan, N. Reyren, A. Fert, C. Panagopoulos, *Nature* **539**, 509 (2016)
118. J.D. Sau, R.M. Lutchyn, S. Tewari, S. Das Sarma, *Phys Rev Lett* **104**, 040502 (2010)
119. M. Sato, Y. Takahashi, S. Fujimoto, *Phys Rev B* **82**, 134521 (2010)
120. G.C. Ménard, S. Guissart, C. Brun, R.T. Leriche, M. Trif, F. Debontridder, D. Demaille, D. Roditchev, P. Simon, T. Cren, *Nat Commun* **8**, 2040 (2017)

Publisher's Note

Springer Nature remains neutral with regard to jurisdictional claims in published maps and institutional affiliations.